Atmos. Chem. Phys., 13, 8505–8524, 2013
www.atmos-chem-phys.net/13/8505/2013/
doi:10.5194/acp-13-8505-2013

Atmospheric Chemistry and Physics Open Access

A net decrease in the Earth's cloud, aerosol, and surface 340 nm reflectivity during the past 33 yr (1979–2011)

J. Herman[1,2], M. T. DeLand[3,2], L.-K. Huang[3,2], G. Labow[3,2], D. Larko[3,2], S. A. Lloyd[5,2], J. Mao[4,2], W. Qin[3,2], and C. Weaver[4,2]

[1]Joint Center for Earth Systems Technology (JCET) Center, University of Maryland, Baltimore County, Catonsville, MD 21228, USA
[2]NASA Goddard Space Flight Center, Greenbelt, MD 20771, USA
[3]Science Systems and Applications (SSAI), Inc., Lanham, MD 20706, USA
[4]Earth System Science Interdisciplinary Center (ESSIC), University of Maryland, College Park, MD 20740, USA
[5]Wyle Science, Technology and Engineering, Houston, TX 77058, USA

Correspondence to: J. Herman (jay.r.herman@nasa.gov)

Received: 17 October 2012 – Published in Atmos. Chem. Phys. Discuss.: 13 December 2012
Revised: 25 June 2013 – Accepted: 12 July 2013 – Published: 27 August 2013

Abstract. Measured upwelling radiances from Nimbus-7 SBUV (Solar Backscatter Ultraviolet) and seven NOAA SBUV/2 instruments have been used to calculate the 340 nm Lambertian equivalent reflectivity (LER) of the Earth from 1979 to 2011 after applying a common calibration. The 340 nm LER is highly correlated with cloud and aerosol cover because of the low surface reflectivity of the land and oceans (typically 2 to 6 RU, reflectivity units, where 1 RU = 0.01 = 1.0 %) relative to the much higher reflectivity of clouds plus nonabsorbing aerosols (typically 10 to 90 RU). Because of the nearly constant seasonal and long-term 340 nm surface reflectivity in areas without snow and ice, the 340 nm LER can be used to estimate changes in cloud plus aerosol amount associated with seasonal and interannual variability and decadal climate change. The annual motion of the Intertropical Convergence Zone (ITCZ), episodic El Niño Southern Oscillation (ENSO), and latitude-dependent seasonal cycles are apparent in the LER time series. LER trend estimates from 5° zonal average and from 2° × 5°, latitude × longitude, time series show that there has been a global net decrease in 340 nm cloud plus aerosol reflectivity. The decrease in $\cos^2$(latitude) weighted average LER from 60° S to 60° N is 0.79 ± 0.03 RU over 33 yr, corresponding to a 3.6 ± 0.2 % decrease in LER. Applying a 3.6 % cloud reflectivity perturbation to the shortwave energy balance partitioning given by Trenberth et al. (2009) corresponds to an increase of 2.7 W m^{-2} of solar energy reaching the Earth's surface and an increase of 1.4 % or 2.3 W m^{-2} absorbed by the surface, which is partially offset by increased longwave cooling to space. Most of the decreases in LER occur over land, with the largest decreases occurring over the US (-0.97 RU decade^{-1}), Brazil (-0.9 RU decade^{-1}), and central Europe (-1.35 RU decade^{-1}). There are reflectivity increases near the west coast of Peru and Chile (0.8 ± 0.1 RU decade^{-1}), over parts of India, China, and Indochina, and almost no change over Australia. The largest Pacific Ocean change is -2 ± 0.1 RU decade^{-1} over the central equatorial region associated with ENSO. There has been little observed change in LER over central Greenland, but there has been a significant decrease over a portion of the west coast of Greenland. Similar significant decreases in LER are observed over a portion of the coast of Antarctica for longitudes −160° to −60° and 80° to 150°.

1 Introduction

The Earth's energy balance is mostly determined by the shortwave solar energy received at the Earth's surface, absorbed by the atmosphere and reflected back to space, and the fraction of longwave energy emitted to space. Both the incoming solar radiation, which includes near-ultraviolet (NUV), visible, and near-infrared (NIR) wavelengths, and the emitted outgoing longwave infrared radiation (IR) are

affected by the presence of clouds and aerosols. Clouds can simultaneously reflect shortwave radiation back to space before it reaches the Earth's surface (resulting in cooling) and act as a thermal blanket to trap longwave radiation (heating) in the lower atmosphere. One of the key questions concerning global warming is the response of clouds as surface temperatures change. Many model studies showing temperature increases indicate a positive feedback for clouds reflecting energy back to space (IPCC, 2007) – that is, as the average temperature increases cloud cover decreases so that more solar energy reaches and is absorbed by the Earth's surface, which is partially offset by increased outgoing IR radiation. It is generally agreed that there has been a statistically significant increase in global average temperature since 1979. An estimate of the increase is 0.15 °C decade^{-1} (Hansen et al., 2010), or about 0.5 °C since 1979. However, in response to the temperature increase, the direction of cloud feedback based on observations is still an open question.

The global heat flow can be partitioned approximately as 341 W m^{-2} average incoming solar radiation, 102 W m^{-2} reflected back to space, and 239 W m^{-2} from outgoing longwave radiation (Kiehl and Trenberth, 1997; Trenberth et al., 2009; Stevens and Schwartz, 2012). Of the 102 W m^{-2} reflected radiation, 74 W m^{-2} is reflected by clouds and aerosols, 5 W m^{-2} by the molecular atmosphere, and 23 W m^{-2} by the surface. Clouds block some of the longwave radiation that would be emitted back to space, so that a decrease in global cloud amount would increase the amount of solar radiation reaching the Earth's surface (more heating), and increase the amount radiated back to space (more cooling). Depending on the effect of clouds on longwave radiative forcing, a global decrease in cloud plus aerosol reflectivity could cause an increase in net heating. This paper discusses one aspect contributing to the energy balance, namely the change in the 340 nm Lambertian equivalent reflectivity (LER) of the Earth's cloud plus aerosol amounts as seen from space for the past 33 yr (1979 to 2011).

Since the long-term wavelength-integrated top-of-the-atmosphere (TOA) solar irradiance is believed to be relatively stable (to within 0.1 %) over recent history (Kopp and Lean, 2011), small changes in the Earth's albedo can have a significant impact on the net radiation budget affecting climate change. Previous estimates of cloud cover change have been made using the International Satellite Cloud Climatology Project (ISCCP) data archive (Schiffer and Rossow, 1983) derived from visible and IR measurements obtained from a variety of different satellites (polar orbiting and geostationary). The problems of joining the disparate ISCCP data sets, starting in 1979, to produce an accurately calibrated long-term time series needed to estimate changes in shortwave energy reflected back to space has been reviewed by Norris and Slingo (2009). One of their key points is that ISCCP uses "a long series of weather satellites that were not designed to maintain onboard calibration or interface with other satellites."

One of the more accurate cloud data sets is from the CERES instrument starting on TRMM (Tropical Rainfall Measuring Mission) in a low-inclination tropical orbit and continuing on the polar-orbiting TERRA satellite starting in 1999 and Aqua in 2002. Direct comparison of broadband CERES data (300–5000 nm) with the narrowband 340 nm LER is difficult because of wavelength-dependent effects and significant changes in surface reflectivity affecting CERES, but not the 340 nm LER. Two other long-term cloud data sets exist, AVHRR (visible and infrared channels) and HIRS (multiple broadband channels from 3 to 15 microns), which have surface reflectivity sensitivity in addition to diurnal cloud variation from drifting orbits similar to the SBUV/2 (Solar Backscatter Ultraviolet 2) instruments. These data sets have required corrections for the drifting orbits (e.g., Labow et al., 2011; Foster and Heidinger, 2012). An analysis of ISCCP cloud frequency (Wylie et al., 2005) shows a strong decrease over land for latitudes 20° N to 60° N that was not seen in corresponding HIRS observations. ISCCP shows a larger decrease over 20–60° N oceans, while HIRS shows a small increase. Evan et al. (2007) suggest that the long-term decreases in cloud cover reported from the ISCCP data may not be reliable, but are instead related to uncorrected satellite viewing geometry effects.

2 Solar Backscatter Ultraviolet (SBUV) data

In October 1978, the first of a series of well calibrated UV measuring satellite instruments, SBUV (Solar Backscatter Ultraviolet) instrument was launched onboard the Nimbus-7 spacecraft for the purpose of measuring changes in the Earth's ozone amount. The measurements were continued with overlapping data by a series of NOAA SBUV/2 instruments (1985 to present). A summary of these instruments is given in Table 1. The longest wavelength channel, 340 nm with a bandpass Δ of 1.1 nm FWHM (full-width half maximum), was chosen in order to measure radiances with almost no ozone absorption as part of the ozone retrieval algorithm. Backscattered 340 nm radiances also provide a useful measure of cloud plus aerosol reflectivity amount for ice- and snow-free scenes, since it is only minimally affected by changes in the surface (vegetation and ocean color).

SBUV instruments measure nadir-view Earth radiances with a double monochromator scanning sequentially through 12 wavelengths between 252 and 340 nm. Each wavelength sample requires 2 s, and a full scan sequence is completed in 32 s, while the spacecraft moves at 7 km s^{-1}. The radiances used for deriving LER are obtained from the 339.8 Δ1.1 nm (Δ = FWHM) band for the Nimbus-7 SBUV and seven NOAA SBUV(/2) instruments. Both the backscattered radiance I_{refl} and solar irradiance I_{solar} are measured at twelve discrete narrow-bandwidth ultraviolet wavelengths: nominally 256, 273, 283, 288, 292, 298, 302, 306, 312, 318, 331 and 340 nm. The exact operational

Table 1. UV satellite data sets used for 340 nm LER.

1978–1990	Nimbus-7/SBUV	340 nm reflectivity is produced as part of standard processing using a new Antarctic ice radiance in-flight calibration. 14 nadir-viewing orbits per day. Full global coverage once per week. Only a few missing days. Near-noon Sun-synchronous orbit.
1985–2006	NOAA SBUV/2 Series 9, 11, 14	340 nm reflectivity is produced as part of standard processing using a new Antarctic ice radiance in-flight calibration. There are 14 nadir-viewing orbits per day giving full global coverage once per week with only a few missing days. The Equator-crossing times drifted during the instrument's lifetime. A small time of day correction has been applied.
2004–present	OMI	340 nm daily reflectivity is now part of standard processing using pre-flight and in-flight calibration. Very stable instrument. Full global coverage every day. Reflectivity values are available for all wavelengths from 330 nm to 500 nm for a 13:30 Sun-synchronous orbit. However, there is an offset between the UV2 (300–370 nm) and VIS (350–500 nm) detectors. Adding OMI to the SBUV SBUV/2 340 nm time series does not alter the estimate of long-term change in LER.
2002–present	NOAA SBUV/2 series 16, 17, 18, 19	340 nm daily reflectivity using a new Antarctic ice radiance in-flight calibration. There are 14 nadir-viewing orbits per day giving full global coverage once per week with only a few missing days. Near-noon Sun-synchronous orbit for the first 5 yr.

wavelength used for this study varies between 339.75 nm and 339.92 nm for the different instruments with $\Delta = 1.1$ nm. The SBUV/2 instrument field of view is 11.13° × 11.13°, which produces a nadir footprint of 168 km × 168 km (equivalent to 1.5°latitude × 1.5°longitude at the Equator). The earlier Nimbus-7 SBUV (1978–1990) footprint is slightly larger because the satellite flew in a higher orbit. All of the data products are produced from normalized radiances $I_{\mathrm{refl}}/I_{\mathrm{solar}}$ to minimize the effects of instrument calibration changes. The LER zonal average and latitude-by-longitude data and documentation are available at the Goddard DES-DISC (http://mirador.gsfc.nasa.gov/ enter keyword LER).

The SBUV–SBUV/2 data give nearly complete global coverage (80° N to 80° S) every 7 to 10 days for the entire 33 yr period, consisting of 19.2 million individual observations taken by the seven instruments, or a mean of 68 independent LER observations per 5° latitude band per day with some overlap between instruments. After applying a common calibration (discussed below), overlap data are averaged together to form a single daily 33-year time series of 340 nm LER. Five of the instruments (NOAA-16, -17, -18, -19 SBUV/2, and OMI) continued to take daily observations into 2012, of which the first 3 are used to estimate long-term change in LER. For those SBUV/2 instruments that had drifting orbits (slowly changing Equator-crossing times), large-scale diurnal changes in LER were minimized (Labow et al., 2011) by correcting to noon values.

The TOMS (Total Ozone Mapping Spectrometer) instruments (Nimbus-7/TOMS (NT) and Earth Probe TOMS (EP)) are not included in the combined 33 yr LER data set because of remaining problems with the photomultiplier detector hysteresis effects (NT) and scan mirror degradation (EP). The hysteresis effect concerns the emergence of a photomultiplier tube instrument from night into bright daylight scenes, where the photomultiplier tube's anode has not had time to thermally equilibrate. Hysteresis effects for the SBUV series were not as severe, and have been corrected. By the time that the SBUV instrument gets to the Northern Hemisphere (NH), the photomultiplier gain is fully stabilized, and the hysteresis effect is gone. The uncertainty of the hysteresis correction in the Southern Hemisphere (SH) is 0.5 % of albedo, or 0.2 RU in the average LER. This is much less than the LER trends estimated from the measured radiance albedo.

The Ozone Monitoring Instrument (OMI) onboard the AURA spacecraft is a hyperspectral CCD instrument that also is used to measure 340 nm LER. This study does not include the OMI 340 nm LER in the LER trend analysis in order to keep the type of observation consistent for the entire 33 yr (i.e., all with the same nadir footprint and bandpass). An extended analysis including OMI data shows that it does not significantly change the 340 nm LER trend results.

The 340 nm derived reflectivity data set provides an alternate estimation for the effect of cloud plus aerosol cover to that provided by the ISCCP, HIRS, and AVHRR data records. There are key differences in the data sets: (1) the 340 nm LER is not significantly affected by the ground or ocean reflectivity ($R_{\mathrm{G}} < 0.06$) compared to visible or NIR wavelengths. (2) The satellites are all of the same type (nadir-viewing polar-orbiting SBUV and SBUV/2), which are all able to see the Arctic, Antarctica, and Greenland for in-flight calibration or calibration validation. (3) Some of the SBUV/2 instruments were compared with the accurately calibrated Space Shuttle SBUV (SSBUV) flown 8 times between 1989 and 1996. (4) The quantity measured, LER, is a direct measure of energy

reflected from the surface, clouds, and aerosols. (5) The LER data are corrected for diurnal variation in cloud cover in a manner that does not remove long-term changes. (6) Unlike ISCCP, the SBUV LER data are not able to separate the different types of clouds, do not separately give optical depth and cloud fraction, and cannot separate clouds from aerosols or snow and ice.

The previous shorter-period LER trend estimates (Herman et al., 2009, 2010) were based on measured radiances at 380 Δ0.5 nm from Nimbus-7/TOMS (N7T) and at 412 Δ20 nm from SeaWiFS (SW). Prior to recalibrating the SBUV and SBUV/2 instruments, it was shown that most of the major reflectivity features were commonly observed at times when there was overlap between the instruments (Herman et al., 2009; Fig. 8). However, the relative calibration between the various satellite instruments was inadequate for the estimation of long-term trends over the entire data record. For the overlap period 2001 to 2006, NOAA-16 SBUV/2 was shown to agree closely with the zonal average trend estimates from SeaWiFS (1997 to 2008). Finally, latitude $\times$ longitude trend estimates were made for N7T and SeaWiFS (Herman et al., 2009; their Fig. 13), which showed significant LER decreases over land areas in the Northern Hemisphere as well as some localized increases in the equatorial Pacific Ocean and near the west coast of South America. However, there are also significant LER differences between the two observing periods based on N7T (380 Δ0.5 nm) and SeaWiFS (412 Δ20 nm), which may partly depend on instrumental characteristics. Since the SBUV and SBUV/2 are the only series of instruments having very similar observing characteristics, span the entire data record 1979 to present, and have a new common calibration, the LER time series (80° S–80° N), and noon corrected time series (60° S–60° N), are constructed entirely from their recalibrated measured radiances.

3 Satellite instrument calibration

The primary measured quantity used in all derived products is the ratio of nadir-viewed backscattered Earth radiances to measured solar irradiance at each wavelength. Solar irradiance is measured by deploying a diffuser to reflect sunlight into the entrance slit of the monochromator as the satellite crosses the terminator into the night side. As a result, many factors in the instrument sensitivity calibration are canceled in the ratio of measured Earth radiances to measured solar irradiance (directional albedo) used for the LER retrieval. The solar diffuser is the only element not common to the optical path in the two measurements. Characterizing changes in diffuser reflectivity is a key element in determining time-dependent calibration changes.

Each SBUV instrument was calibrated in the laboratory prior to launch. The prelaunch calibration procedures include measuring and characterizing the monochromator wavelength scale and band pass, electronic offset, photomultiplier tube (PMT) output inter-range gain ratios, thermal response, nonlinearity, radiance and irradiance sensitivity, solar diffuser reflectivity, and diffuser reflectivity angular dependence (Frederick et al., 1986). The radiance and irradiance calibrations are traceable to standard NIST (National Institute of Standards and Technology) quartz-halogen tungsten-coated filament (FEL) lamps and diffuser BRDF (bidirectional reflectance distribution function) standards (e.g., Huang et al., 1998; Georgiev and Butler, 2007). These measurements are performed using the same laboratory configuration (Fegley and Fowler, 1991). The only difference between the radiance and irradiance calibration is the use of a laboratory diffuser deployed in the same position as the solar diffuser used for in-flight solar irradiance measurements. Therefore, the albedo calibration (ratio of radiance sensitivity to irradiance sensitivity) depends only on the diffuser BRDF characterization rather than the lamp irradiance standard.

On-orbit validation of the albedo calibration for the earlier SBUV/2 instruments is based, in part, on coincidence analysis with SSBUV data from eight flights between 1989 and 1996. Each SSBUV flight had both pre-launch and post-launch laboratory calibrations traceable to laboratory BRDF standards. The laboratory standards for the SSBUV-6, SSBUV-7, and SSBUV-8 flights were also used for all SBUV/2 instruments from NOAA-14 onward, and are designed to be more accurate than previous standards (Janz et al., 1995). In the present LER study, NOAA-11 albedo calibration is revised to be consistent with SSBUV-6; the N7-SBUV and NOAA-9 albedo calibrations are adjusted to the current laboratory standard, based on the coincidence radiance comparison with NOAA-11.

The prelaunch albedo calibration can also be validated on-orbit using measurements of Antarctic ice plateau regions, as described by Jaross and Warner (2008). NOAA-17 and NOAA-19 LER values over Antarctica are in good agreement with NOAA-11 and NOAA-14 measurements (after adjustments based on SSBUV coincidences in March 1994 and January 1996). NOAA-16 and NOAA-18 LER values were found to be approximately 6 % lower than concurrent NOAA-17 data, so their calibrations were adjusted upwards. Further details are given in DeLand et al. (2012).

Nimbus-7 SBUV and Nimbus-7 TOMS radiance measurements were originally observed to be as much as 10 % low when emerging from darkness in the SH. This behavior, termed "hysteresis", was caused by a delay in the PMT anode reaching thermal equilibrium from exposure to the backscattered radiances. A correction was developed for Nimbus-7 SBUV by comparing PMT signals with concurrent data from a reference diode that does not have this problem. Nimbus-7 TOMS did not have a reference diode. DeLand et al. (2012) provides additional details about the correction procedure, which has an uncertainty of approximately 0.5 %. The impacts on LER data are mainly at polar latitudes in the SH, but can extend to the Equator during SH winter. Since NOAA-9

measured the 340 nm radiance with PMT cathode output at solar zenith angles SZA less than 80 degrees, its 340 nm LER data are not affected by hysteresis, but have other uncharacterized anomalies that reduce its accuracy. The procedures to correct NOAA-9 anomalies and the Nimbus-7 SBUV hysteresis problem over Antarctica are given in detail by DeLand et al. (2001, 2012).

The SBUV/2 instruments use emission lines from an onboard mercury lamp to monitor diffuser reflectivity changes in orbit (Weiss et al., 1991), as well as changes from prelaunch laboratory values compared to those obtained in-orbit. Errors in the goniometric calibration of the diffuser can also be evaluated and corrected using solar irradiance measurements (Ahmad et al., 1994). All instruments from NOAA-11 onward have used this system to monitor the time-dependent change of the albedo calibration in orbit. For Nimbus-7 SBUV and NOAA-9 SBUV/2, an alternate procedure involving more frequent solar exposures was developed to characterize diffuser changes (Schlesinger and Cebula, 1992), which was less reliable than the onboard calibration system.

The analysis of 340 nm radiance measurements over Antarctic snow/ice-covered regions provides additional validation for the albedo calibration time dependence, as described by Huang et al. (2003) and DeLand et al. (2012). For NOAA-14 and NOAA-16, the snow/ice radiance results agree with the onboard calibration system within their combined long-term uncertainty (∼1 %). For NOAA-11, NOAA-17, and NOAA-18, the snow/ice radiance results are used for the time dependence calibration of the 340 nm channel, which is also validated in the ozone product analysis (DeLand et al., 2012).

Standard calibration procedures were developed for estimating ozone amounts based mostly on ratios of UV wavelengths (306, 312, 318, and 331 nm). While the calibration procedures were also applied to 340 nm radiances, a new comparison of the overlapping 340 nm LER time series from different SBUV SBUV/2 instruments over the Antarctic Plateau showed that there were still differences. To remove these differences, we assume that there has been no long-term change in the reflectivity of the Antarctic Plateau, over the 33 yr period of our data set, to establish the final calibration for each instrument represented in the LER product. The average LER for each instrument was calculated during each SH summer season (December–January) mostly in the solar zenith angle range SZA = 60° to 70°. When satellite orbit drift makes this SZA range unavailable in some years, we calculated the seasonal average LER values using SZA = 70°to 78° and scaled this value to 60° to 70° conditions using a linear fit for SZA 60° to 80° measured during the satellite's first year in orbit. Four of the SBUV instruments used have absolute calibrations that are directly traceable to NIST standards, either through prelaunch calibration (NOAA-17 and NOAA-19) or through SSBUV coincidence analysis (NOAA-11 and NOAA-14). The average

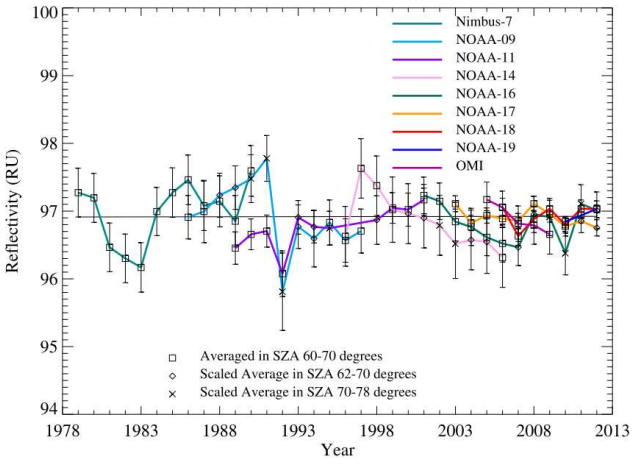

Fig. 1. Normalized summer Antarctic snow/ice LER at 340 Δ1.1 nm averaged between SZA 60° and 70° degrees. Squares: LER averaged over 60° < SZA < 70°. Diamonds: LER averaged over 62° < SZA < 70°. X: LER averaged over 70° < SZA < 78° and interpolated from the first year of data back to the range LER averaged over 60° < SZA < 70°. The average LER for each satellite is adjusted to 96.92 RU based on the best-calibrated four SBUV/2 instruments. The error bars are derived from the standard deviation of the points describing the envelope of the LER data combined with the annual standard deviation from the mean.

of all summer LER values was calculated from these four instruments to define a reference Antarctic LER value of $R_{\text{avg}} = 96.92$ RU with a standard deviation of 0.51 RU (where 1 RU = 0.01 = 1.0 %). NOAA-11 data from 1992 were excluded from this calculation to remove the effects of the Mt. Pinatubo volcanic eruption. Small adjustments (typically less than ± 0.5 %) were then made to each instrument's calibration so that its average Antarctic LER value also equaled R_{avg}. A linear fit to all adjusted Antarctic LER values (excluding 1992 data) gives a long-term trend of 0.00 ± 0.20 RU over 33 yr, as shown in Fig. 1. This result shows that the calibration uncertainty is sufficiently small to permit determining zonal average decadal trends larger than $0.2/3.3 = 0.06$ RU decade^{-1} at other latitudes.

4 Lambertian equivalent reflectivity (LER)

Lambertian equivalent reflectivity R is calculated by requiring that the measured depolarized normalized radiance I_{SM} matches the calculated normalized radiance I_{S} at the observing position of the satellite (Eq. 1) by adjusting a single free parameter R in the formal solution of the radiative transfer equation (Chandrashekar, 1960; Herman et al., 2001).

$$I_{\text{S}}(\Omega, \theta, R, P_{\text{O}}) = \frac{R I_{\text{d}}(\Omega, \theta, P_{\text{O}}) f(\Omega, \theta, P_{\text{O}})}{1 - R S_{\text{b}}(\Omega, P_{\text{O}})} + I_{\text{d0}}(\Omega, \theta, P_{\text{O}}) = I_{\text{SM}}, \quad (1)$$

where

– Ω = ozone amount

- θ = viewing geometry (solar zenith angle, satellite look angle, azimuth angle)
- R = LER at P_O ($0 < R < 1$)
- P_O = pressure of a surface with reflectivity R at the local ground altitude.
- S_b = fraction scattered back to P_O from the atmosphere
- I_d = sum of direct and diffuse irradiance reaching P_O
- f = fraction of radiation reflected from P_O reaching the satellite
- I_{dO} = radiance scattered back from the atmosphere for $R = 0$ and $P = P_O$

The units of reflectivity are frequently given in percent that is defined as 0 % for a completely absorbing dark surface and 100 % for a totally reflecting surface. To avoid confusion between absolute reflectivity with relative percent changes in reflectivity, the LER is expressed in "reflectivity units", or RU, rather than percent ($0 < \text{LER} < 100$ RU).

Satellites with comparatively large FOVs, such as the $180 \times 180\,\text{km}^2$ FOV for SBUV and $168 \times 168\,\text{km}^2$ for SBUV/2, containing a mixture of sub-pixel views of the surface and clouds, tend to appear Lambertian because of the blurring and averaging of geometric features. Satellites with small FOVs (e.g., $1 \times 1\,\text{km}^2$ from MODIS) are likely to resolve major cloud and surface irregularities, instead of averaging over them, so that the resolved features may not exhibit Lambertian behavior.

All of the radiative transfer calculations are performed using plane-parallel geometry with spherical geometry corrections applied for all solar zenith angles. To avoid errors in the correction, the data are limited to SZA $\leq 80°$. For the SBUV and SBUV/2 series, the viewing angle is always 0°(nadir viewing). Shadows of elevated cloud decks upon the lower clouds may lower the apparent LER for a given cloud amount as a function of latitude and season. Other situations, such as thin multilayer cloud decks can increase the LER because of interlayer reflections. Because of this, the LER is not a measure of cloud + aerosol amount, but rather an estimate of the amount of energy reflected back to space or transmitted T to the Earth's surface (approximately $T = (100 - R)/(100 - R_G)$) (Herman et al., 2009), where R_G is the 340 nm LER of the Earth's surface.

Previous studies have used BUV-type instruments to compile climatologies and time series of LER or estimated minimum surface LER (SLER) (Herman and Celarier, 1997; Herman et al., 2001, 2009; Kleipool et al., 2008) as a function of location and month. In the absence of snow or ice, the UV surface LER is typically well below 10 RU. These studies have shown that the LER over land is generally 2–4 RU in the NUV (340–380 nm), and up to 10 RU in small desert regions such as in Libya. There is little seasonal variation in NUV land reflectivity compared to the visible and NIR wavelengths except in the presence of snow/ice. LER over ocean varies from 4 to 6 RU, with small regions of up to 9 RU. Lower ocean LERs correlate with regions of phytoplankton growth, as chlorophyll *a* and other aquatic chromophores that absorb in the NUV. Higher ocean reflectivities correlate with comparatively clear ocean water. An estimate of the global average surface LER for scenes without snow or ice is about 5 RU based on Herman and Celarier (1997) using N7 TOMS data.

Histograms for LER frequency of occurrence for typical scenes are given in Herman et al. (1997) and Kleipool et al. (2008), with the lowest occurrences corresponding to nearly aerosol- and cloud-free scenes. While it is difficult to obtain completely cloud-free scenes with a large satellite footprint (relative to the size of individual clouds or mesoscale cloud formations), the minimum values of LER are taken as a slight overestimate of surface reflectivity as observed from space over many years of daily data. Instruments with a higher spatial resolution (smaller FOV), such as OMI or MODIS, are statistically more likely to provide cloud-free scenes through the gaps between cloud formations than SBUV or TOMS.

The 340 nm nadir-viewing observations in this study assure that the satellite look or viewing angle is uniform and free of specular reflection (Sun glint). A depolarizer on the instruments removed sensitivity to Rayleigh scattering polarization effects (Heath et al., 1975). Data in the zonal average trend analysis are restricted to 60° N–60° S so as to remove most of the effect of persistent snow/ice cover, although snow and ice are still a factor in the high-northern-latitude boreal winter months. There is almost no land at high southern latitudes, 45° S–60° S, upon which snow can accumulate. The effect of surface winds affecting ocean wave brightness (white caps) is included in the calculated LER.

LER represents the *combined* cloud, aerosol (including haze) and surface scene reflectivity as observed from space. Changes in LER are mostly caused by clouds and, to a lesser extent, aerosols, except in regions covered by snow/ice (e.g., Greenland). While the local details vary from day to day, the global patterns of cloud cover are present every day. Most of the regional cloud patterns repeat seasonally, but with small shifts in latitude and longitude. An example of LER from a single day, 10 September 2008, is shown in Fig. 2 using the daily imaging capabilities of OMI. The LER in Fig. 2 is scaled from 0 to 80 RU showing some bright high clouds in the equatorial region, a bright hurricane cloud in the Gulf of Mexico (a category 4 hurricane named Ike), and the geographic distribution of cloud cover. The main patterns are from cloud cover showing higher area-averaged LER towards the polar regions, an equatorial band of clouds at about 5° N, and local minima (more cloud-free) at about 20° N and 20° S. Some of the smaller features are frequently recurring, such as the cloud plumes going southeastward from Argentina, southern Africa, and Australia. Significant sulfate

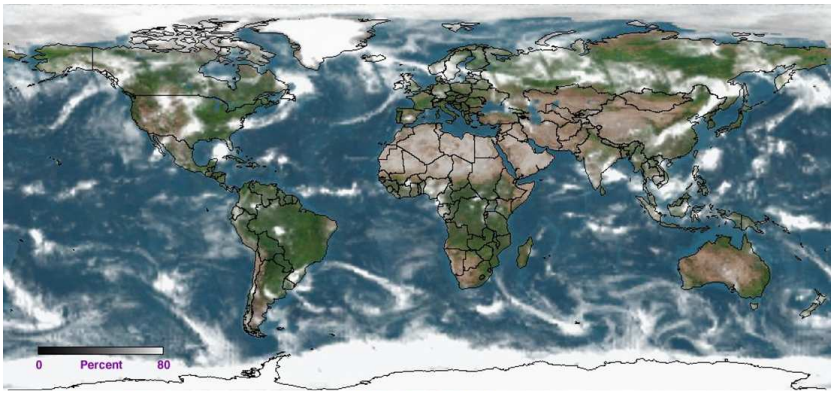

Fig. 2. The geographical distribution of 340 Δ1.1 nm LER from AURA/OMI for 10 September 2008. The hurricane in the Gulf of Mexico is a Category 4 Hurricane named Ike. The LER data (see black, grey, and white, scale lower left) are superimposed on a MODIS clear-sky color map. The high-altitude storm cloud in the Gulf of Mexico has higher reflectivity (whiter) than midlatitude clouds.

aerosols, which typically rise to an altitude of 3–5 km when well away from their sources, can sometimes increase the nadir-viewing LER of a scene up to 15 RU relative to a clear-sky background. Soot, smoke, desert dust, volcanic ash, black carbon and organic aerosols absorb in the NUV and can decrease the scene reflectivity.

While there is substantial daily variability in both cloud amounts (fraction of area covered) and patterns, the general seasonal reflectivity features repeat each year with small shifts in location. These small shifts in location lead to large monthly and yearly change in ground-based cloud amount time series, and can also lead to long-term systematic trend errors that are not present in space-based observations. In addition to changing cloud patterns, there are some quasi-cyclic features related to atmospheric oscillations (e.g., the 2.3 yr Quasi-Biennial Oscillation, QBO, and the more irregular El Niño and La Niña Southern Oscillations). These oscillations have well-known effects on weather, so that their long-term secular changes are of interest in climate studies.

The combined 33 yr 340 nm SBUV LER data record has been used to show that reflectivity related to the amount of cloud cover varies systematically as a function of time throughout the day, with a minimum near noon over the oceans and a maximum during the afternoon over land (Labow et al., 2011). The corresponding effects of LER diurnal variability that arise from different SBUV/2 instruments operating at different local times have been partially removed by correcting the data to noontime values. Maximum correction of LER values to their noon-normalized equivalents is typically less than 2 RU.

5 Zonal average LER

The 340 nm radiance data used to form the zonally averaged LER time series in 5° bands were derived from newly recalibrated production files for the SBUV instruments. Aside from the new Antarctic ice radiance common calibration, *no smoothing or adjustments have been made to make the LER values agree at overlapping times at other latitudes*. When the satellite data sets overlap, the LER values are averaged using equal weights. The combined zonally averaged time series are shown in Fig. 3 for every other 5° latitude band for both hemispheres and all the latitude bands in Fig. 4. There are some missing data at high southern latitudes caused by the drifting orbits of the earlier SBUV/2 satellites.

In the equatorial region represented by 17.5° N to 17.5° S, the annual maxima occur in June in the NH and in January in the SH. This corresponds to the clouds following the annual motions of the Intertropical Convergence Zone (ITCZ). Once outside of the ITCZ at 27.5°, the annual cycle weakens, especially in the SH. In the NH there is a relatively small peak caused by winter cloud conditions occurring over the land. From 30° N to 60° N, the annual cycle is dominated by land conditions with heavy cloud cover plus snow in the winter causing a maximum LER in January. The corresponding 30°–60° zone in the SH is more complicated. There is a weak winter signal from 35° S to 40° S with an LER maxima occurring in June. In the 45° S to 50° S the annual cycle is dominated by the ocean cloud cover with little coherent annual cycle. Finally, at higher latitudes 55° S to 60° S the annual cycle reappears, but with the maxima occurring in the spring (October–November) with maximal cloud amount after winter cooling (Haynes et al., 2011). This region corresponds to the southern polar vortex wind system, associated with the Antarctic ozone hole, which maximizes in areal extent in September–October and breaks up in October to November.

Figure 4 shows an alternate representation of the multiyear zonal average LER variability and annual cycles based on monthly averaged data. The figure shows the lack of symmetry between the NH and SH with a local June maximum at 7.5° N (green) and the minimum LER at about 17.5° in each hemisphere. The phasing of the annual maxima and

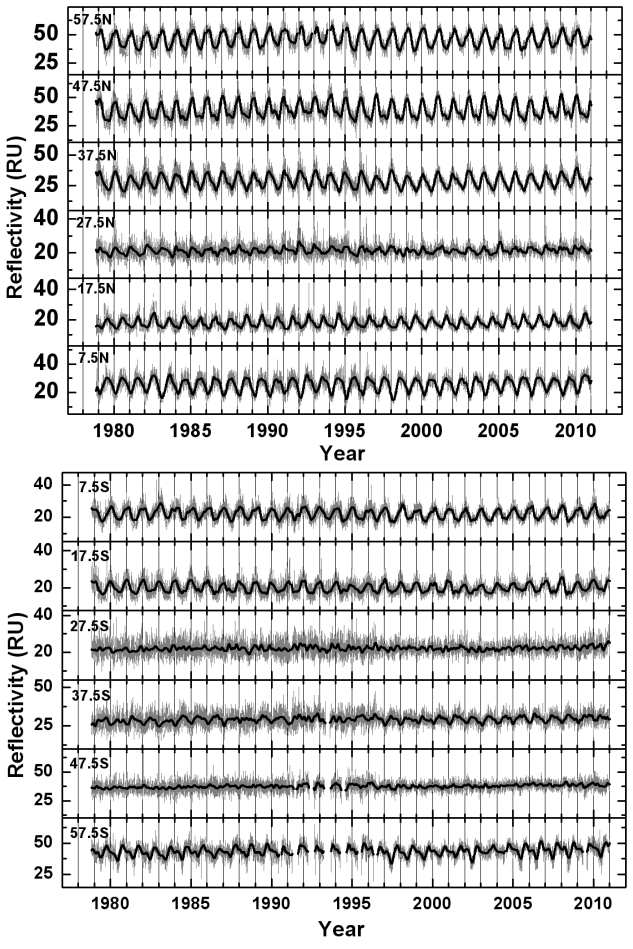

Fig. 3. LER zonal average time series for twelve 5° bands from 57.5° S to 57.5° N (1979–2010). The light grey color corresponds to daily LER, while the black solid lines are a 30-day low-pass filter of the daily data.

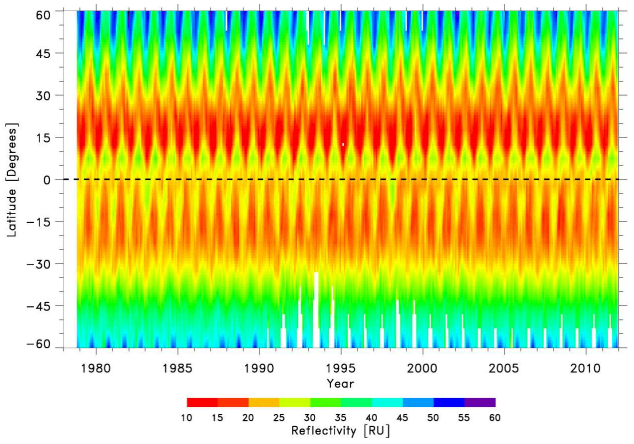

Fig. 4. Zonal mean monthly averages of LER 1979–2011 for all latitudes between 60° S and 60° N showing the seasonal patterns as a function of latitude. White is missing data.

minima shifts as a function of latitude. The largest LER are in the near-polar regions, with the annual average LER in the Southern Hemisphere larger than that in the Northern Hemisphere.

Figure 5a shows the 33 yr annual average noon-normalized zonal average reflectivity as a function of latitude for 3 cases (land and ocean, land only, ocean only). The land-only case is limited to 60° N to 35° S, ending near the tip of South Africa, because of insufficient land at latitudes between 35° S and 60° S. All three cases show the equatorial region having a pronounced hemispherical asymmetry (a maximum at 7.5° N and two minima at 17.5° N and 22.5° S). The noon-normalized data are limited to the latitude range to $\pm 60°$ in Fig. 5a, whereas the seasonal OMI LER (Fig. 5b) is in a near-noon orbit (13:30 local Equator-crossing time) and can be extended to $\pm 85°$. The 7.5° N offset maxima corresponds to the ITCZ, which has annual mean position between 5° N and 10° N but shifts northward during boreal summer and southward during boreal winter. The two minima at 17.5° N and 22.5° S correspond to the subsidence side of Hadley circulation dominated by the subtropical high-pressure belts. The reflectivity difference in the two minima are related to the ratio of land to water in the two hemispheres, with oceans having more persistent low, nonprecipitating cloud cover than land, mainly on the west side of continents with underlying cold ocean currents. There are only minor differences between the 3 cases in Fig. 5a. The ocean areas in the NH (15° N–60° N) have higher reflectivity than the land areas, indicating more average cloud cover. In the equatorial region (Equator to 15° S) there is higher cloud reflectivity over land than over oceans. For the region between 15° S and 30° S, the cloud reflectivity over oceans is higher than over land. The latitudinal dependence of the LER curve in Fig. 5a is similar to the CERES-reflected shortwave flux (Stevens and Schwartz, 2012, their Fig. 9). Figure 5b shows the seasonal variation of the zonal average reflectivity as derived from 4 yr of OMI 340 Δ1.1 nm LER data. During the NH summer and autumn months (May to October) the local equatorial LER maximum is located at about 8° N and shifts to about 4° N during the winter and spring months (November to April). During the NH winter (December to February) LER is higher than in the summer (June to August) from 25° N to 80° N, and has a larger difference than in the SH winter (June to August) compared to the SH summer (December to February). The hemispheric differences in the seasonal behavior of the LER are caused by the much smaller land-to-ocean ratio in the SH.

There is a strong correlation of the equatorial LER (5° S–5° N) with the multivariate El Niño Southern Oscillation index (MEI) (Wolter and Timlin, 1993, 1998), which can be found at http://www.esrl.noaa.gov/psd/enso/mei/table.html. MEI is composed from a principal component analysis of a combination of six variables: (1) sea-level pressure, (2) zonal

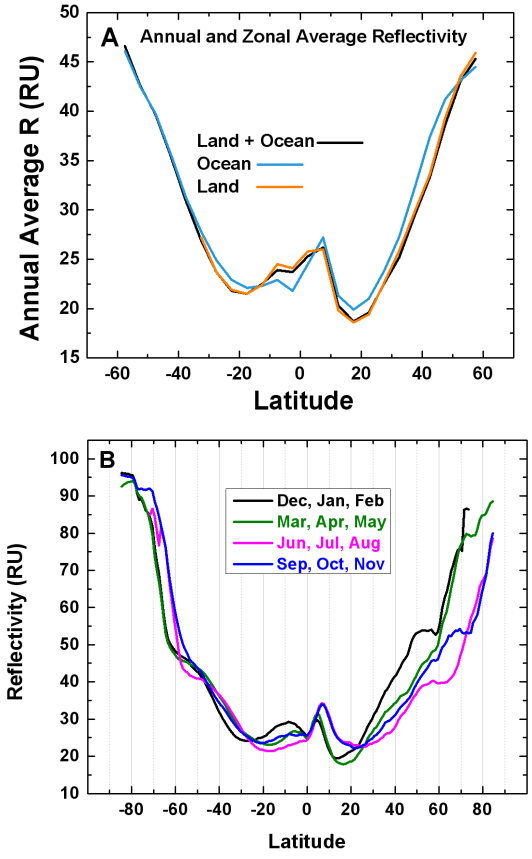

Fig. 5. (A) Thirty-three-year average of the noon-normalized zonal average time series as a function of latitude from the SBUV series of instruments separated in to land only, ocean only, and combined. **(B)** Four-year seasonal average of OMI LER data (black: December–February; green: March–May; magenta: June–August; blue: September–November).

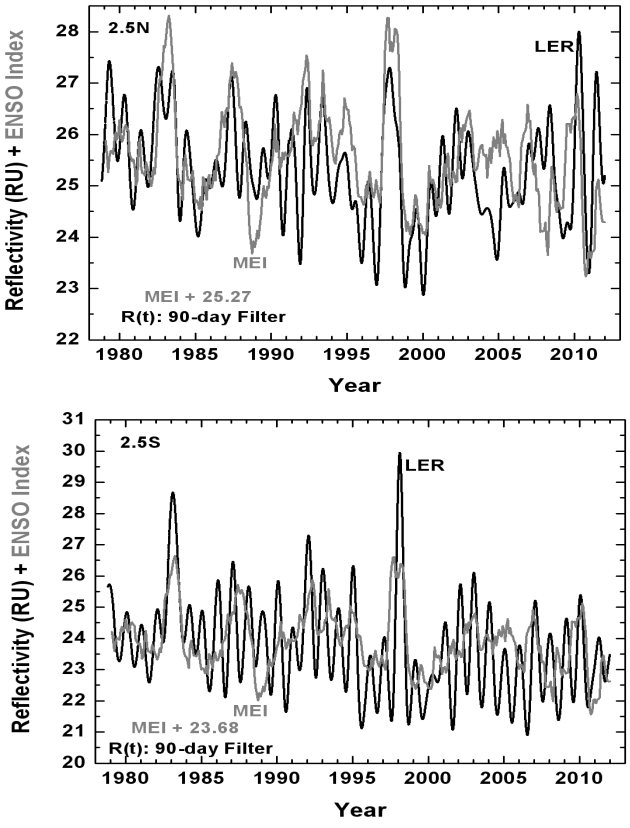

Fig. 6. A comparison of the LER (black) with the scaled MEI + R_{AVG} (grey) for the latitude bands 0 to 5° N (top) and 0 to 5° S (bottom). The LER is a 90-day low-pass filter of the daily LER time series.

and (3) meridional components of the surface wind, (4) sea surface temperature, (5) surface air temperature, and (6) total cloudiness fraction of the sky. Figure 6 shows a comparison between the equatorial cloud cover in two zonally averaged LER time series for the bands 0° to 5° N and 0° to 5° S. The daily LER data are time filtered by using a 90-day low-pass filter to correspond with the MEI data. In Fig. 6 the MEI data (approximately in the range MEI = ± 3) are shifted by adding the constant 33 yr average LER to the MEI (MEI+23.68 at 5° N and MEI + 25.27 at 5° S) to overlap with LER.

The correlation of the 0–5° N LER with the MEI is very high for major ENSO events in 1982–1983, 1986–1987, 1991–1992, 1997–1998, and 2010–2011. High correlations occur from 1979 to 2002, after which the correlation breaks down with an apparent anticorrelation in 2005 and 2008, during the period when ENSO occurred every year. The anticorrelation between the equatorial zonal mean LER and MEI can be attributed to the differences in spatial pattern between the central Pacific types of ENSO (2004–2005 and 2006–2007 El Niño) and the eastern Pacific types of ENSO (2005–2006 and 2007–2008 La Niña) (Kao and Yu, 2009; Singh et al., 2011), with the positive correlation resuming in 2010. Over the period 1979 to 2011 the decadal pattern of variability of the MEI and LER are similar. For example, there is an apparent upward trend in the LER from 2000 to 2010 that also appears in the MEI. The matching of the long-term patterns between LER and MEI strongly suggests that the observed LER changes are not instrumental artifacts, but instead represent real physical changes in cloud plus aerosol reflectivity. A similar comparison for the zonal region 0–5° S shows a weaker 90-day correlation with MEI except for the two major ENSO events. However, the longer-period (5 yr) correlation is apparent.

The volcanic eruptions from El Chichon (April 1982) and Mt. Pinatubo (June 1991) inserted large amounts of particulates into the atmosphere that were easily observable over a wide range of latitudes, especially at sunrise and sunset for a year after the eruptions. To see if these effects are in the LER time series, the annual cycle was removed from the 30° S to 30° N zonal average LER(30° S–30° N, t) time series by subtracting a

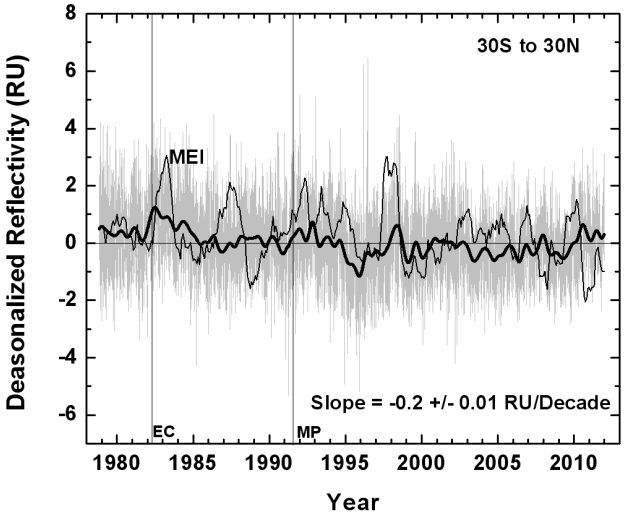

Fig. 7. Deseasonalized LER time series for 30° S to 30° N (grey) with a superimposed 90-day low-pass filter (thick black) and the MEI (thin black). The lines labeled EC and MP represent the dates of the El Chichon (April 1982) and Mt. Pinatubo (June 1991) volcanic eruptions.

best-fit sinusoid as a function of time 21.1327–0.6602 Sin(π (t + 0.5793)/0.50016) RU (t, 0.5793, 0.50016 in yr). Figure 7 shows that the deseasonalized LER(30° S–30° N, t) short-term perturbations are coincident with major volcanic eruptions of El Chichon in 1982 and Mt. Pinatubo in 1991 as well as the major ENSO events represented by the MEI. However, a significant component of the MEI consists of local cloud observations that could also contain volcanic eruption perturbations. The effect of El Chichon and Mt. Pinatubo eruptions on the deseasonalized LER (30° S–30° N, t) cannot be clearly separated from the coincident ENSO events. In addition to the short-term perturbations, the resulting deseasonalized time series has a long-term linear decrease of 0.2 ± 0.01 RU per decade, which would be significant for estimating increases in surface solar insolation related to climate change. In the following section, all zonal average trends are computed for daily deseasonalized data and plotted over the original daily LER data. The trends for the original daily data are almost identical to the daily deseasonalized data.

6 Long-term change in LER

The long-term change in LER(θ, t) for each 5° latitude band centered on θ can be estimated from a linear least-squares fit to each zonal average LER time series or deseasonalized time series. Because of the length of the time series, and the use of complete years, the linear trend of each time series including the annual cycle and the deseasonalized time series are almost identical. The results (Fig. 8) show that there is a major difference in the LER change between the hemispheres. Most of the change occurs in the NH, having more land area compared to the SH with more ocean area. There is also an additional large change in the equatorial region $\theta = 15°$ S to 5° N that is caused by changes in the Pacific Ocean ENSO region near 175° W longitude. The largest NH change, $\Delta R = -0.9$ RU per decade, is near 50° N followed by the change at 30° N–40° N of $\Delta R = -0.7$ RU per decade. A significant contribution to the change in energy reflected back to space comes from the equatorial band between 0° and 15° S (ΔLER $= -0.5$ RU decade^{-1}).

To estimate the effect of reflectivity change on the energy reflected back to space, the zonally averaged LER(θ, t) is weighted by $\cos^2(\theta)$, to account for the decreasing area of higher-latitude bands and for the angle of the incident solar irradiance for $\theta = 60°$ S to 60° N (Eq. (2) and Fig. 9). This simplified weighting neglects the small effect from the seasonal $\pm 23.3°$ tilt of the Earth's rotation axis, which would introduce a 10 % annual cycle to the weighted LER(θ, t). A best-fitting Sin(t) function was subtracted from the data to provide a deseasonalized version (Fig. 9b). A linear least-squares fit gives a decrease in the 60° S to 60° N reflectivity at a rate of 0.24 ± 0.01 RU per decade or a total of about 0.79 ± 0.03 RU since 1979. There are several multiyear cycles apparent in the time series, including one near the end of the times series suggesting that the increase in LER above the least-squares mean during the past few years is temporary.

The average $\cos^2(\theta)$ weighted LER reflectivity (Eq. 2) for $\theta = 60°$ S to 60° N is $< R > = 26.9$ RU for clouds plus aerosols and the Earth's surface. Of this amount, the average reflectivity of the surface is about 5 RU (estimated from Herman and Celarier, 1997), or $< R > = 21.9$ RU for clouds plus aerosols. The change over 33 yr is $\Delta < R > = -0.24 \cdot 3.3 = -0.79$ RU. Assuming that there has been no long-term change in the 340 nm surface reflectivity, the change (0.79 RU) represents a decrease of 3.6 ± 0.2 % of 340 ± 0.55 nm energy reflected back to space by clouds plus aerosols over 33 yr.

$$< R(t) > = \frac{\sum_{-60}^{60} \mathrm{LER}(\theta, t) \cos^2(\theta)}{\sum_{-60}^{60} \cos^2(\theta)} \quad (2)$$

7 A cloud–aerosol reflectivity perturbation to Trenberth et al. (2009) estimate of shortwave surface absorption

To estimate the effect of a 3.6 % decrease in cloud plus aerosol reflectivity in terms of broadband shortwave energy change ΔE absorbed by the surface, we start with the shortwave energy balance given by Trenberth et al. (2009). The shortwave SW portion of the Earth's energy balance model of Trenberth et al. (2009) contains five major factors: (1) energy

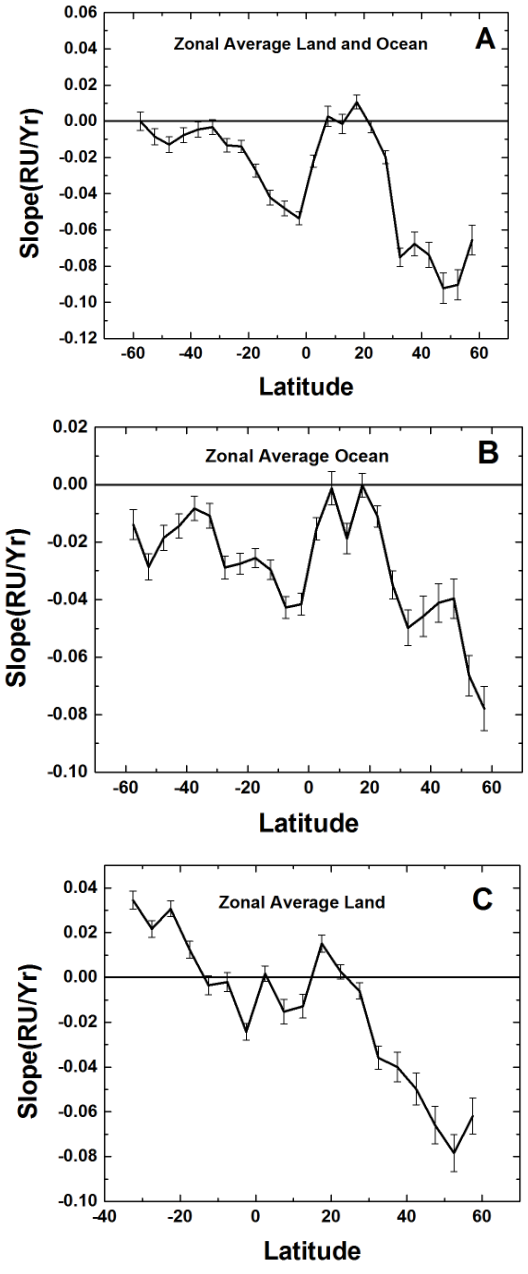

Fig. 8. Zonal average trends (RU yr^{-1}) 1979 to 2011. **(A)** Land and ocean, **(B)** ocean only, **(C)** land only.

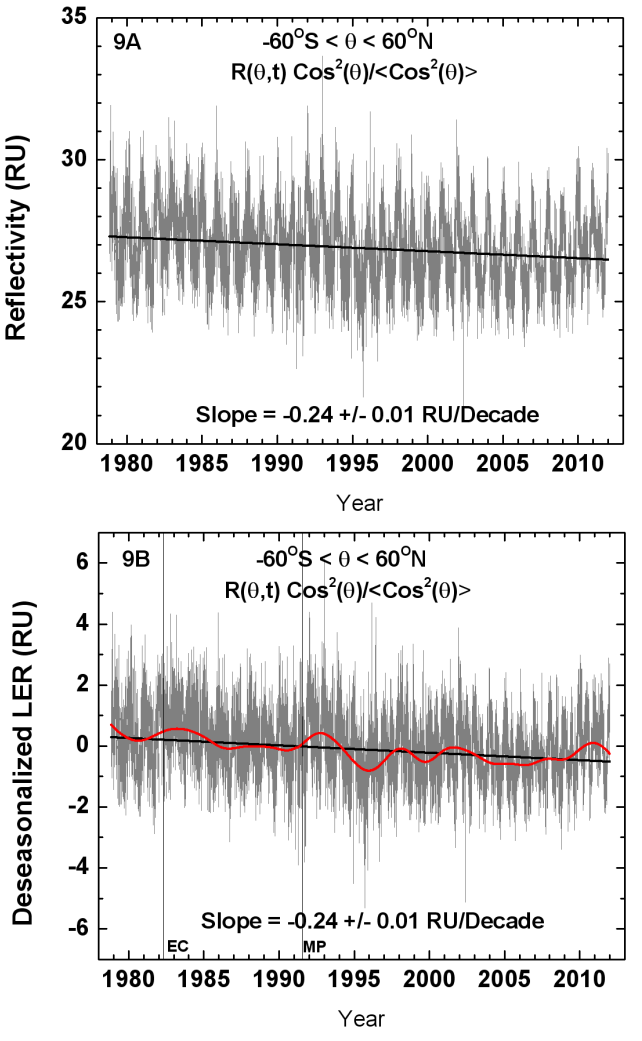

Fig. 9. (A) Normalized $\cos^2(\theta)$ weighted zonal average reflectivity for $\theta = 60°$ S to 60° N, **(B)** normalized deseasonalized LER(θ, t) $\cos^2(\theta)$ for $\theta = 60°$ S to 60° N. The dark solid line is a 365-day low-pass filter showing the major multiyear cycles. Normalization in equation 2 is $< \cos^2(\theta) > = 0.707$. EC = El Chichon and MP = Mt. Pinatubo.

reflected to space by aerosols and clouds, (2) energy reflected by Rayleigh scattering, (3) energy absorbed in the atmosphere, (4) energy reflected by the Earth's surface, and (5) energy absorbed by the Earth's surface. In the following calculation, all physical properties (e.g., surface reflectivity and atmospheric absorption) of the atmosphere and surface are held constant except for cloud reflectivity. We assume the 3.6 % decrease in cloud and aerosol reflectivity is constant as a function of wavelength for this estimation.

To estimate the effect of a 3.6 % decrease in cloud plus aerosol reflectivity in terms of shortwave energy change ΔE absorbed by the surface, we assume as starting values the Trenberth et al. (2009) estimate of 341.3 W m^{-2} average solar energy at the top of the atmosphere, 78 W m^{-2} absorbed by the atmosphere, 79 W m^{-2} reflected by the atmosphere plus clouds and aerosols, and 23 W m^{-2} reflected by the surface (Fig. 10). Rayleigh scattering is assumed to be 6 % of the incident radiation, or 4.74 W m^{-2}. Of the incoming radiation, 79–4.74 = 74.26 W m^{-2} are reflected by clouds and aerosols, giving a fractional cloud plus aerosol reflectivity of 74.26/341.3 = 0.2176. The estimated broadband reflectivity value is close to the fractional 340 nm LER estimate of $< R > = 0.219$. The radiation heading toward the surface

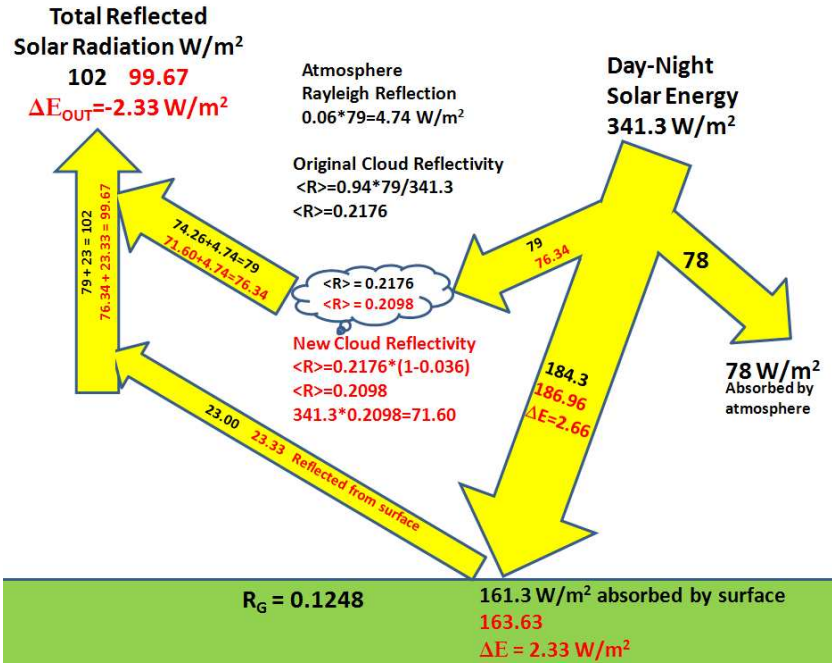

Fig. 10. Shortwave energy balance diagram based on Trenberth et al. (2009). The numbers in black are from Trenberth. The numbers in red are from the effect of perturbing the cloud + aerosol reflectivity $< R >$ by 3.6 % from Trenberth's implied value of 21.76 RU to 20.98 RU. The result is an increase of 1.4 % in energy absorbed by the surface. All other parameters are held constant.

is 341.3−78–79 = 184.3 W m^{-2}, of which 23 W m^{-2} is reflected from the surface, yielding 102 W m^{-2} of total reflected radiation and 161.3 W m^{-2} absorbed by the surface. The effective fractional surface reflectivity based on Trenberth et al. (2009) is $R_G = 23/184.3 = 0.1248$, which is held constant. To make a simplified calculation of the shortwave change ΔE in solar energy absorbed by the surface from the change in cloud and aerosol reflectivity $\Delta < R >$, Trenberth's 78 W m^{-2} estimate of atmospheric absorption is held constant. The calculation is equivalent to one term in a multivariate differential expansion.

For calculating energy change ΔE, the exact starting numbers (i.e., Trenberth et al., 2009) do not make a significant difference. Extra significant figures are retained only for ease in checking the calculations.

The 3.6 % decrease in average cloud plus aerosol reflectivity gives a reduced cloud plus aerosol fractional reflectivity of $0.2176 \cdot (1–0.036) = 0.2098$ giving $341.3 \cdot 0.2098 = 71.60$ W m^{-2}. Then the clouds and atmosphere reflect 71.60+4.74 = 76.34 W m^{-2}, and 341.3−76.34–78 = 186.96 W m^{-2} reaches the surface, a change of 2.66 W m^{-2}. The amount reflected from the surface is now 23.33 W m^{-2}, and 186.96−23.3 = 163.66 W m^{-2} is absorbed by the surface. The total reflected solar radiation is now 76.34+23.33 = 99.67 W m^{-2}. The difference is 99.67−102 = −2.33 W m^{-2}, which is the same as the difference absorbed by the surface, ΔE = 163.63−161.3 = 2.33 W m^{-2}, or a change of 1.4 %.

The net change in shortwave radiation absorbed by the surface, ΔE = 2.3 W m^{-2}, is partially offset by a change in longwave cooling to space arising from the decrease in cloud plus aerosol amount, an increase in thermal energy radiated at the surface caused by a 0.5 °C increase in global average surface temperature since 1979 (Hansen et al., 2010), and changes in tropospheric temperatures. The amount of the longwave offset plus changes in atmospheric absorption determine whether the cloud plus aerosol change represents a net positive or negative feedback. The correlated increase in surface temperature suggests a net positive feedback.

Including the seasonal change in insolation (solar declination changing between ±23.3°), starting with 1361 W m^{-2} at the TOA and the noontime-corrected latitude-by-longitude 340 nm LER for each day since 1979 (Fig. 11) modified by the average diurnal LER variation (Labow et al., 2011), we obtain a nearly identical value of 2.28 W m^{-2} increase in solar radiation absorbed by the Earth's surface over 33 yr.

8 Geographical distribution of LER changes

The SBUV series of nadir-viewing satellite instruments operate in 14 near-polar orbits per day. Complete geographical coverage between 80° S and 80° N can be obtained by combining 10 days of LER data in a 2° × 5° latitude-by-longitude grid. Figure 11 shows each time series long-term linear trend as individual rectangles. The long-term (1979 to 2011) decreases in LER(θ, φ, t) mostly occur over land

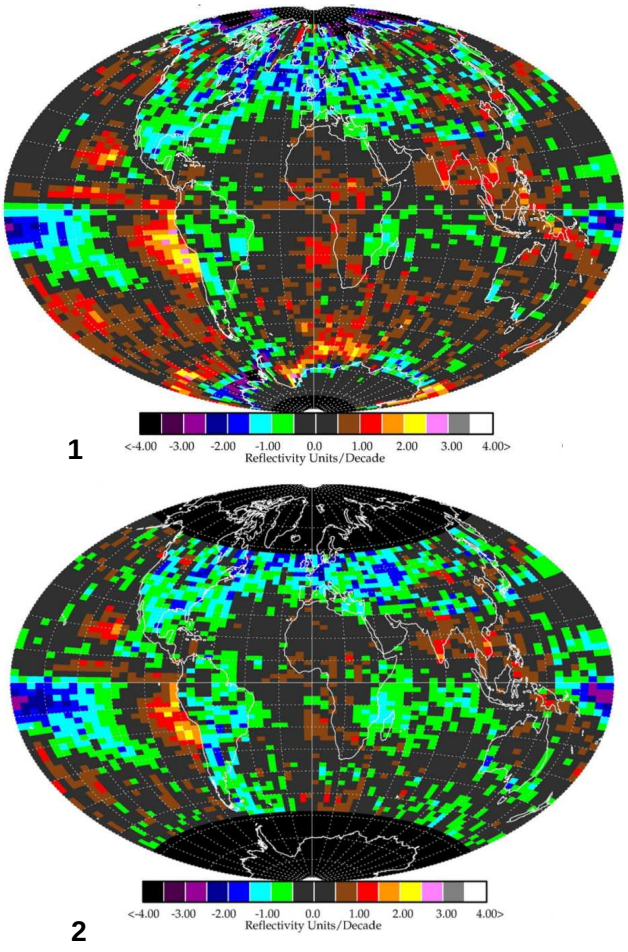

Fig. 11a. LER linear trends $\Delta\mathrm{LER}(\theta, \varphi)$ as a function of latitude θ and longitude φ. Each colored rectangle is the linear slope from individual time series. The upper panel **1** has no time correction applied to the data, while the lower panel **2** is based on LER normalized to noon using corrections derived for combined land and oceans. The noon normalization could not be applied to latitudes $>60°$ because of a lack of measured radiances at different local times.

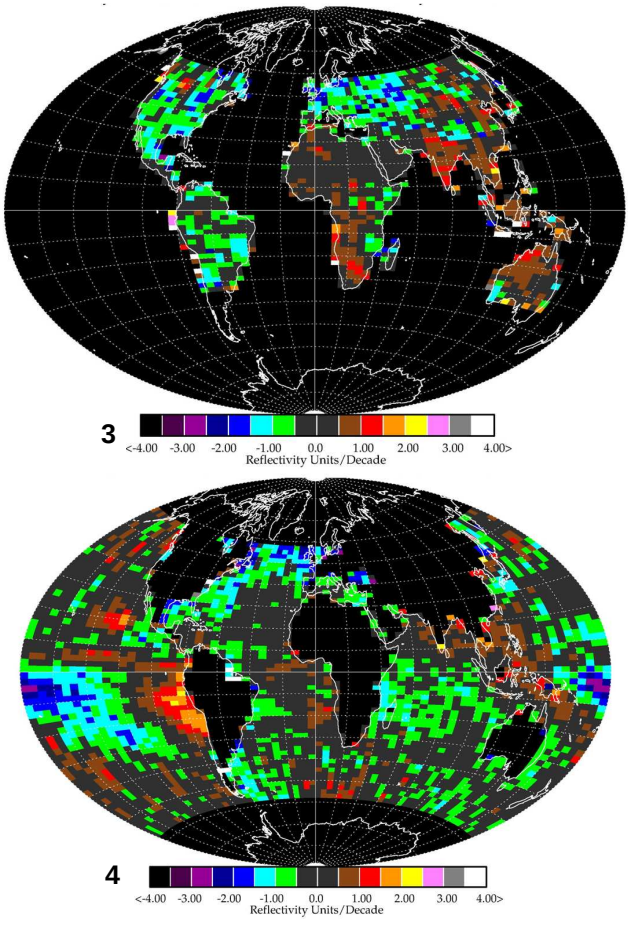

Fig. 11b. LER linear trends $\Delta\mathrm{LER}(\theta, \varphi)$ as a function of latitude θ and longitude φ. The upper panel **3** has land-only zonal average noon normalization corrections applied to the data, while the lower panel **4** is based on ocean-only zonal average noon normalization corrections applied. The noon normalization was not applied to latitudes $>60°$ because of a lack of measured radiances at different local times.

in both the SH and NH, with the largest LER decreases occurring over central Europe. The results suggest a gradual increase in solar energy reaching the ground and longwave cooling to space since 1979 for these regions. In contrast with LER decreases over adjacent land areas, LER change over the nearby Pacific Ocean ranges from local increases to areas where the changes are statistically not different from zero. The clear separation for $\Delta\mathrm{LER}(\theta, \varphi)$ between adjacent land and ocean areas indicates that the observed zonal average LER decreases are not from the SBUV and SBUV/2 calibration issues. The decrease of cloud cover from eastern Asia over the Pacific Ocean largely dissipates before reaching the middle of the Pacific Ocean. The same is not the case over the much smaller area of the North Atlantic Ocean, where the prevailing west-to-east winds transport continental cloud cover over the ocean. This means that the decreases in cloud amount over the northern US and Canada can also be seen over the North Atlantic.

The noon-normalized time correction (Labow et al., 2011) could not be applied at high latitudes above 60° in Fig. 11a panel 2 because of insufficient diurnal data from the satellites. Figure 11b uses zonally averaged normalized time corrections that were shown to be different over land (panel 3) and oceans (panel 4). While the effect of using separate land and ocean time corrections on LER changes has an effect on their regional distributions, the general patterns are similar. In both the uncorrected and noon-normalized LER data there have been no changes observed over most of central Africa, with a small decrease in LER over southeastern Africa near Madagascar. The land regions showing the largest LER increase are in India and Indochina. Australia and New Zealand are largely unchanged. North and South

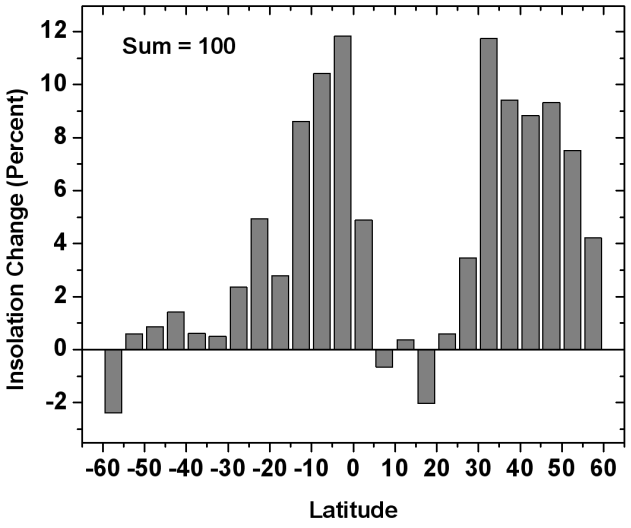

Fig. 12. Percent change in 340 nm surface solar insolation as a function of latitude normalized to sum to 100.

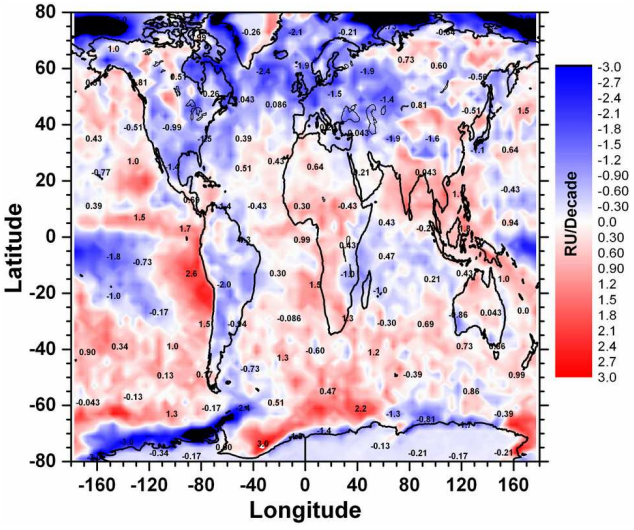

Fig. 13. Contour plot of latitude × longitude trends showing major areas of change in RU decade^{-1} based on the LER non-noon-normalized trend data in Fig. 11a (upper panel **1**). LER trends smaller than |0.3| RU decade^{-1} are not statistically significant from zero. The area-averaging contour plot shows trend details that are not obvious in panels 1 and 2 of Fig. 11a. The LER trend numbers on the map refer to contour boundaries and not the colored areas represented by the scale.

America show a significant decrease in LER. There are interesting $\Delta\mathrm{LER}(\theta, \varphi)$ features over the oceans related to clouds that appear to be associated with ocean currents. Cloud cover has increased over the region where the Humboldt Current impacts the western coast of South America in the region between 10° S and 20° S. There is a similar increase off the west coast of North America associated with the California Current and in the Pacific region just north of the Equator at 5° N and a large region of decrease just south of the Equator near 170° W to 170° E. A smaller feature appears near Indonesia and runs southward to just northeast of Australia.

The percent distribution of 340 nm surface solar insolation change with latitude is shown in Fig. 12 based on changed 340 nm transmission $\Delta\mathrm{T} = -\Delta\mathrm{R}/(1 - R_\mathrm{G})$ for $\cos^2(\theta)$ weighted $\mathrm{LER}(\theta, t)$. Most of the estimated change comes from the latitude bands from 15° S to 0° (31 %) and from 25° N to 60° N (36.3 %). If the 340 nm LER changes are caused by global warming, and if similar changes are associated with longer wavelengths, then the LER change may represent a positive cloud plus aerosol feedback that amplifies the warming effect over land in the NH, parts of the SH, and the north polar region (Fig. 11a panel 1 and the contour plot, Fig. 13).

Figure 13 is based on the non-noon-normalized LER data (Fig. 11a panel 1) in order to extend to higher latitudes $>|60°|$. In the Arctic region, the LER data are from April to August, and the Antarctic region LER data are from October to February, so that the trends shown near the Arctic and Antarctic regions (Figs. 11a and 13) are representative of late-spring to summer months. The uncertainties in local LER trends are larger than for the zonal average trends estimates because of far fewer data points in the local areas. Each local box in Fig. 11 ($2° \times 5°$) contains only 4 points per 10 days (144 points per year). The Fig. 13 contour plot effectively averages over the variance of adjacent pixels in Fig. 11. Figure 13 shows many local features with large enough trends to be statistically significant with a high degree of confidence ($\Delta|\mathrm{LER}| > 0.3$ RU per decade). The calculated LER trends shown in Fig. 13 over the Antarctic continent have small formal errors, but a lower degree of confidence because of fewer data points per year (<60). Similar trend uncertainties apply to the individual LER-trend pixels (Fig. 11 panel 1) in the Arctic region, which includes Greenland. On the Fig. 11 color scale, the LER-trend pixels over most of Greenland and Antarctica are colored black representing zero. Figure 13 also shows that the average LER change over central Greenland is essentially zero, while there are larger changes, negative and positive, on the western and eastern coasts, respectively. In the Antarctic, there are significant changes in LER over the coastal region (negative for longitudes −160° to −60° and 80° to 150°, and positive from −50° to 50° and 150° to 170°).

The SBUV instrument calibration method using Antarctic snow/ice reflectivity selects only the high plateau region that is sufficiently away from the coastal line to avoid the changing weather and sea ice. The SBUV calibration region is effectively an average over a large number of $2° \times 5°$ pixels such that the average trend for each SBUV instrument is zero over its lifetime (typically 5 to 10 yr). This short-term averaging does not preclude a small residual long-term trend on individual pixels, or on the contour plot average over a small

set of pixels. The small 33 yr LER trends shown in Fig. 13 (-0.13, -0.17, and -0.21 RU decade^{-1}) over the Antarctica high plateau are equivalent to zero (see the color scale) within the level of statistical significance.

Since the maximum amounts of daily surface solar insolation occur at latitudes poleward from the Arctic (and Antarctic) circle during summer, long-term decreases in LER (increases in surface solar insolation) may contribute to decreasing ice amounts. However, the LER cannot separate changes in ice reflectivity from changes in cloud reflectivity. If the observed LER decreases are partly caused by areal decreases in ice reflectivity, the change still represents less energy reflected back to space and more solar energy absorbed by the surface.

9 Regional LER time series and trends

Major areas of change are shown in the Fig. 13 contour plot (RU decade^{-1}) for the latitude range from 80° S to 80° N based on the non-noon-normalized LER trend data in Fig. 11a panel 1. While the contour plot represents the same data as in Fig. 11a panel 1, the alternate representation shows additional regional features that are difficult to see in a plot of the individual time series trends. The Fig. 13 scale ranges from -3 to 3 RU per decade (blue to red) with a few black areas at high latitudes off-scale to show details at other latitudes. The indicated trends are for the contours between colors and not for the colored areas.

9.1 General features

The Pacific Ocean land boundary in North and South America (Fig. 13) shows a clear separation between positive (increasing LER over the ocean) and negative trends (decreasing LER over the land). As mentioned earlier, such a latitude-independent separation between land and ocean (negative over land and positive over ocean) suggests the trends are not instrumental artifacts related to calibration. The zonal average negative LER trend in the NH (Fig. 8) is driven by the negative changes over large land areas of North America and Europe, plus the North Atlantic Ocean, which is not offset by the positive changes over the Pacific Ocean. In the SH, only South America shows a decreasing LER, which is offset by increasing LER over the oceans and other land areas (e.g., Africa and Australia).

In the ocean region near Antarctica extending from 160° W to 50° W (near the Palmer Peninsula) there is a strong region of LER decrease (more than 2 RU decade^{-1}) that may be associated with cloud and sea-ice change. Further east, the trend reverses over the ocean and becomes an LER increase between 40° E and 40° W. In all cases, these ocean area changes follow the continental ice boundary with almost no change over the continental ice between 70° S and 80° S.

While the land plus ocean zonal average LER (Fig. 8a) shows a decrease between 20° S and 35° S, the zonal average SH over land (Fig. 8c) between 20° S and 35° S shows an increase in LER caused by the changes in Africa, southern Asia, Malaysia, and Australia. Between 10° S and 10° N the zonal averages are dominated by the changes off the west coast of Peru and in Malaysia, and the semi-permanent band of clouds just north of the equator.

In India there is a general increase in LER that stops abruptly at the start of the Himalayan Mountains. Part of the increase just south of the Himalayan Mountains may be associated with increasing blowing dust and biomass burning (see Figs. 2 and 3 in Gautam et al., 2009). Just north of the start of the Himalayan Mountains there is a decrease in LER extending over the high mountain regions, which could be associated with decreasing cloud amounts and decreasing snow cover (Gurung et al., 2011). The region of decrease extends into southern China (Tibetan Plateau region) and southwards to the northern part of Vietnam. There is a region of increased LER centered on 40° N in China, extending from the Beijing area westward into Tibet to about 75° E. Some of the increasing LER regions in China and India may be partly caused by increasing amounts of aerosols from industrial pollution (e.g., Beijing–Shanghai region and parts of middle and southern India). Away from the coastal area in China, the shape of the region of increased LER follows the outlines of the Gobi and Taklamakan desert regions.

At higher NH latitudes (>40° N), there is a notable decrease in LER over Hudson Bay and on the west coast of Greenland between 60° N and 70° N of as much as 2 RU decade^{-1}. This trend goes to near zero (statistically insignificant) over central Greenland, increases on the west coast (1.2 RU decade^{-1}) and reverses on the east coast of Greenland (-1.2 to -2 RU decade^{-1}). The ocean areas around Greenland show strong decreases in cloud cover (-2 RU decade^{-1}) extending into the Arctic region. The result is increased surface insolation on the ocean and possibly on east coast ice areas at high latitudes during the late-spring and summer months. Alternately, part of the decrease in LER could be from darkening of ice reflectivity associated with melting. To the east, the decreasing cloud cover extends over England (-2 RU decade^{-1}) and over much of Europe. Specific time series are shown for a few key areas in larger latitude × longitude boxes (less trend uncertainty) in Figs. 14–17.

9.2 Mid-Pacific Ocean

Figure 14 shows a 90-day low-pass filter LER time series (black) for a portion of this region bounded by the box 1° S–9° S, 157° W–177° W along with the MEI (grey) showing significant correlation for most LER events. The correlations with MEI are similar to those in Fig. 6 except that the local LER decreases (2 ± 0.1 RU decade^{-1}) are much larger than for the equatorial zonal average (0.5 RU decade^{-1}).

Table 2. LER Trends at locations in Fig. 17.

Location name	Latitude	Longitude	LER trend (RU decade^{-1})
Europe	45° N to 51° N	7.5° E to 17.5° E	−1.35
United States	31° N to 49° N	117.5° W to 82.5° W	−0.97
Canada	49° N to 53° N	127.5° W to 72.5° W	−0.38
Madagascar	19° S to 13° S	42.5° E to 47.5° E	−1.14
Atlantic west of Africa	25° S to 13S	2.5° W to 2.5° E	+0.64
Southern India	11° N to 19° N	72.5° E to 77.5° E	+0.89
Equatorial Pacific Ocean	1° S to 9° S	157° W to 177° W	+2.1
South America land	11° S to 29° S	42.5° W to 67.5° W	−0.9
South America ocean	11° S to 29° S	82.5° W to 102.5° W	+0.8
Southeast Asia	11° S to 29° S	42.5° E to 72.5° W	+0.5

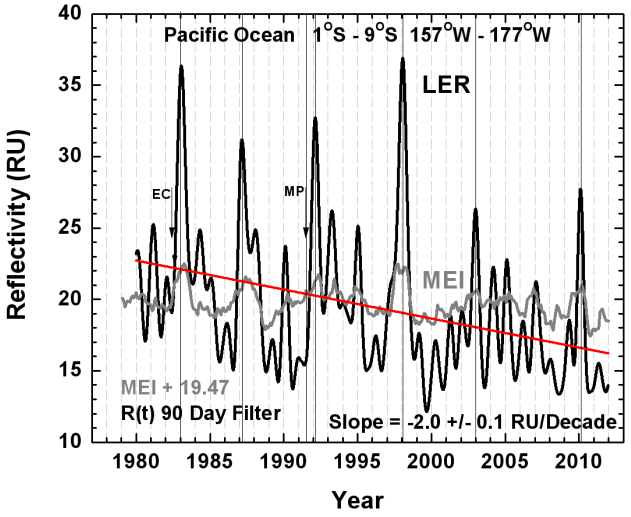

Fig. 14. LER time series (Black) compared with the offset MEI + 19.47 (grey) for the Pacific region shown in Fig. 11 that has a large reflectivity change.

The time series appears to be dominated by peaks occurring in 1983, 1987, 1992, and 1998, which could affect the estimated linear slope. The MEI time series also has a slope of -0.2 ± 0.05 per decade. After removing the slope from the multivariate ENSO index to obtain MEI_D, and then creating the function $\mathrm{LER}_D = \mathrm{LER} - 4\mathrm{MEI}_D + 19.47$, the major peaks are removed and the new slope is estimated as -2.1 ± 0.1 per decade, which is approximately the same as before. The 33 yr decreasing reflectivity trend associated with the ENSO events (Figs. 11 and 14) suggests that there may be a long-term change in the underlying ocean currents in the equatorial region. Since 2000 the LER and MEI suggest a decrease in the frequency of major ENSO events. The larger peaks in LER and MEI after 2000 (2003 and 2010) are significantly smaller than the four earlier peaks. The decrease in LER during the past three decades (Fig. 12) is consistent with the observed decrease in equatorial precipitation and cloud cover in the central Pacific (0 to 10° S, 150° E to 120° W) during 1979 to 2010 (Gu and Adler, 2013).

9.3 Additional sites

LER trends from additional wide area sites (Fig. 18) selected from regions with significant change shown in Fig. 13 are given in Figs. 15 to 16 and Table 2 along with maps taken from Google Earth.

9.4 South America

Similar multiyear patterns appear in the South American LER time series (Fig. 15) with opposite trends over the ocean (0.8 ± 0.1 RU decade^{-1}) and over land (-0.9 ± 0.2 RU decade^{-1}). The small corner extending over the Atlantic Ocean does not alter the estimated trend. The trend over land is similar to those for North America (Table 2). Two smaller regions (14° S–18° S, 75° W–85° W and 18° S–24° S, 75° W–80° W) entirely over the oceans near the coasts of Peru and Chile have trends of 1.6 ± 0.3 RU decade^{-1} and 2 ± 0.3 RU decade^{-1} for the period 1979 to 2011. There has been a statistically significant decrease in LER trends when including the N7-SBUV period from 1979 to 2011 (1.6 and 2 RU decade^{-1}) and the trends omitting this period, 1988 to 2011 (1.4 and 1.3 RU decade^{-1}). These trends are shown in Fig. 17 for the two ocean areas west of Peru for the periods 1979 to 2011 and for 1988 to 2011.

For coastal regions that have large diurnal variations in cloud amount, application of the zonal average correction does not remove the diurnal variation of the observations caused by the changing Equator-crossing time of the SBUV/2 instruments. Since similar positive trends occurred using the shorter time series from N7-TOMS (1979–1992), which had a nearly constant near-noon Equator-crossing time (Herman et al., 2001, Plate 1), it suggests that the existence of a positive trend is not caused by aliasing from diurnal variation.

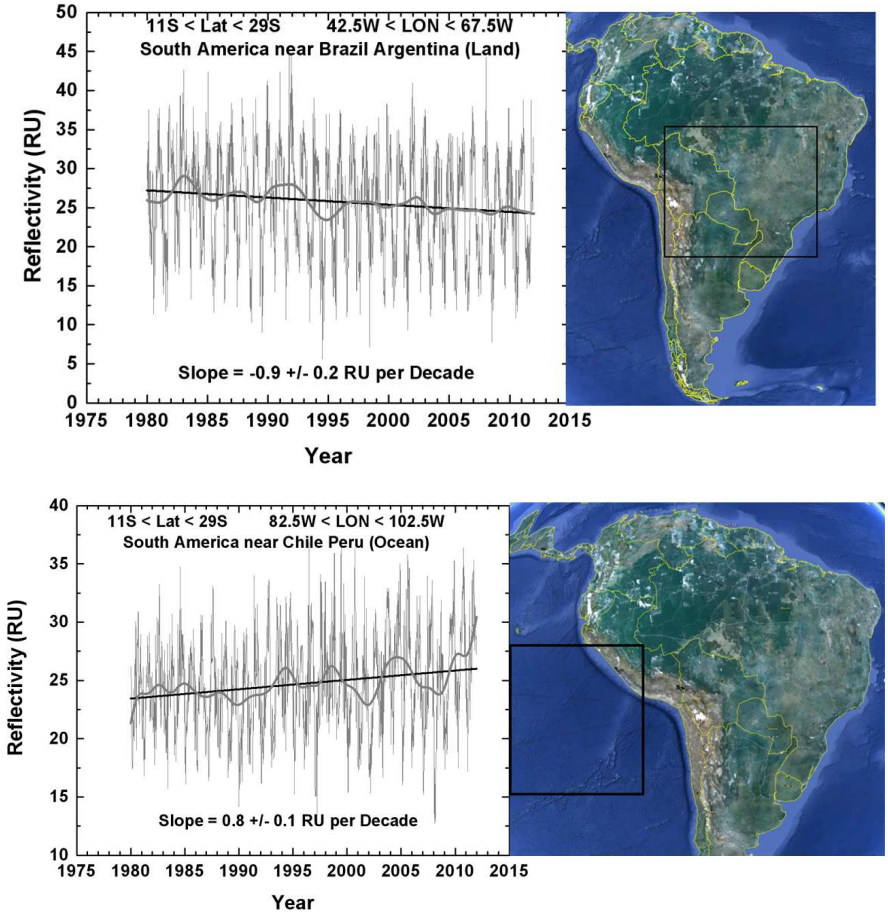

Fig. 15. LER(θ, φ) and ΔLER(θ, φ) for the indicated latitude $\times$ longitude boxes showing the decrease in LER over land and the increase over a small region of Chile and Peru. Both daily data and 365-day low-pass filter are shown.

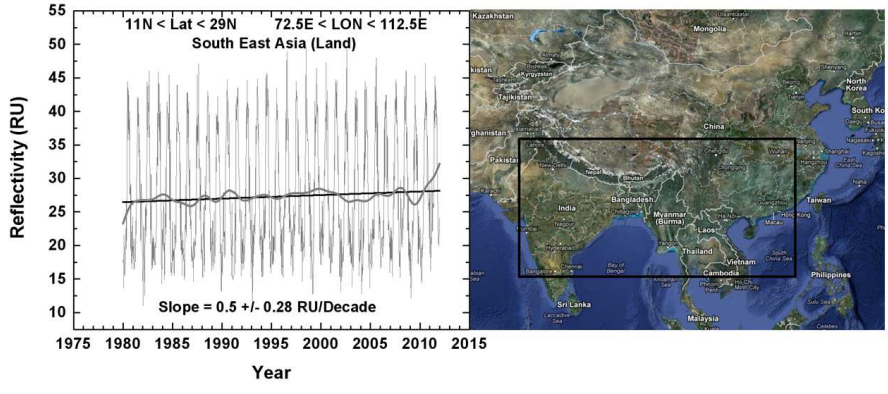

Fig. 16. LER(θ, φ) and ΔLER(θ, φ) for the indicated latitude $\times$ longitude box showing the increase in LER over India, southern China, and Indochina. Both daily data and 365-day low-pass filter are shown.

9.5 India, southern China, and Indochina

There is an increase in LER of 0.5 RU decade^{-1} over a wide region indicated by the box drawn in Fig. 16 that implies a decrease in sunlight reaching the surface. Specific areas within this region (e.g., southern India, Table 2) have larger increasing trends (0.89 RU decade^{-1}) than the area average. The increasing LER is consistent with the observed increase in rainfall in the Asian monsoon region (Gu and Adler, 2013).

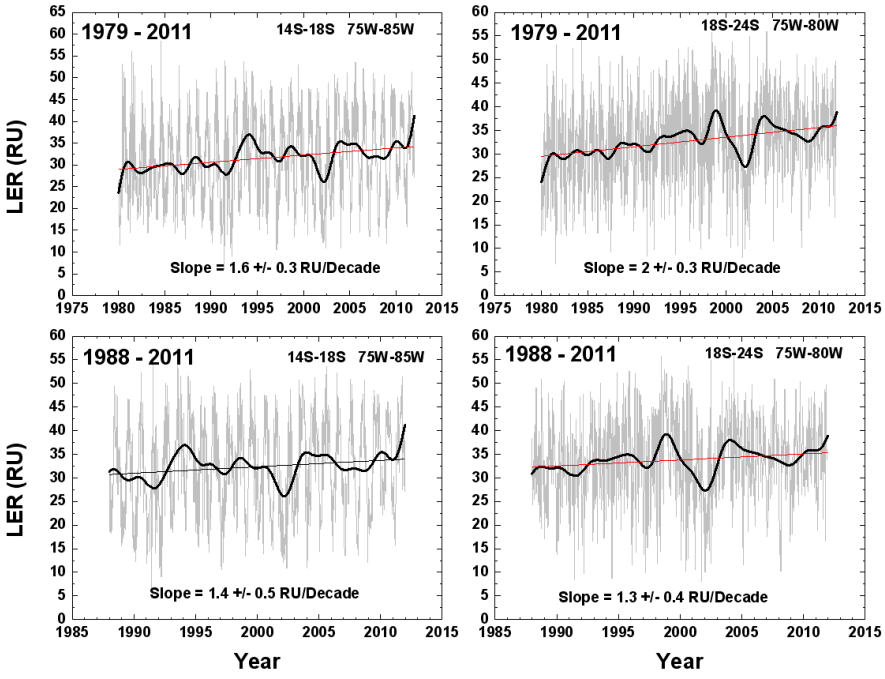

Fig. 17. Comparison of change in LER associated with Peruvian maritime stratus for the period including N7-SBUV (1979 to 2011) and without N7-SBUV (1988–2011) for two Pacific Ocean locations west of Peru (14° S–18° S, 75° W–85° W; and 18° S–24° S, 75° W–80° W).

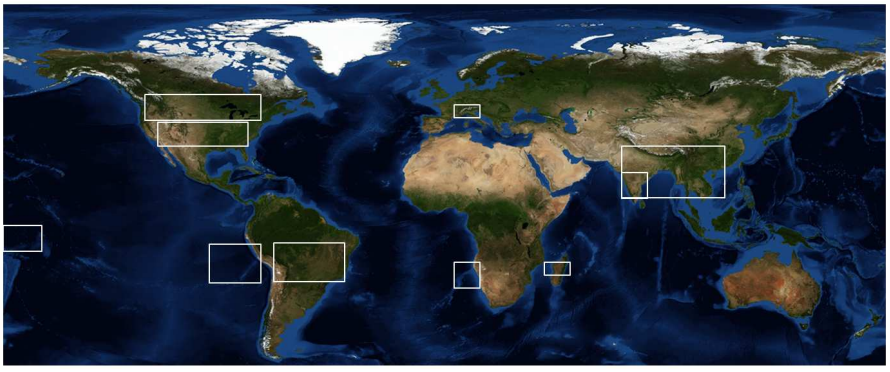

Fig. 18. Rectangular boxes represent interesting locations of selected sites for estimating LER trends based on the latitude × longitude trend maps shown in Fig. 11. The map is based on the Suomi National Polar-orbiting Partnership (SNPP) Visible Infrared Imaging Radiometer Suite (VIIRS).

9.6 LER trends at various locations

Table 2 contains a list of LER trends at various locations shown in Fig. 18.

10 Summary

This study shows that a consistent common calibration and identical retrieval algorithm applied to seven SBUV instruments over 33 yr are sufficient to detect long-term changes in cloud plus aerosol reflectivity that can be differentiated from seasonal or instrumental differences. This is partly demonstrated by the comparison of the 340 nm LER with the mulitvariate ENSO index (MEI), which showed high correlation for the larger ENSO events, especially in 1982–1983 and 1991–1992. The estimated trends in LER are a function of location, with little or no trend over the Pacific Ocean areas adjacent to the decreasing LER trend over North America. Similar differences occur on the west coast of South America. The clear difference between adjacent land and ocean areas shows that the trends are neither instrument artifacts nor incorrect calibrations over the 33 yr period. The 60° S to 60° N change in cosine^2 (latitude) weighted average LER, which can be used for approximating changes in energy reflected

back to space from changes in LER, shows a global weighted average change of −3.6 % over 33 yr. Perturbing the shortwave energy partitioning from Trenberth et al. (2009) by a 3.6 % decrease in cloud plus aerosol reflectivity gives an increase in the amount of shortwave solar energy reaching the surface of 2.7 W m^{-2}, and an estimated increase in shortwave energy absorbed by the surface and decrease of shortwave energy reflected back to space of 2.3 W m^{-2} (a 1.4 % change). The LER change is unevenly distributed as a function of latitude and longitude, with the largest decreases in LER occurring over land in the NH and over the North Atlantic Ocean. The LER trend contour plot (Fig. 13) suggests that there has been little observed change in LER over central Greenland, but that there has been a significant decrease in LER over the west coast of Greenland and a small region of increase on the east coast. Similar significant decreases in LER are observed over a portion of the coast of Antarctica for longitudes −160° to −60° and 80° to 150°. There are significant areas over India, southern China, and Indochina where the LER has increased (decreased surface insolation), a large increase on the west coast of South America that is in the region where the Humboldt Current impacts the South American continent (Peru and Chile), and a large decrease in LER in the equatorial mid-Pacific Ocean near 170° W to 10° E longitude. The decrease in LER is consistent with an increase in surface solar radiation reaching the Earth's surface, which was also observed in the global surface radiation network since 1990 (Wild et al., 2005; Pinker et al., 2005).

Acknowledgements. This research is supported by the NASA MEaSUREs Project. The data and documentation are available at the Goddard DES-DISC (http://mirador.gsfc.nasa.gov/ enter keyword LER).

Edited by: J. Quaas

References

Ahmad, Z., DeLand, M. T., Cebula, R. P., Weiss, H., Wellemeyer, C. G., Planet, W. G., Lienesch, J. H., Bowman, H. D., Miller, A. J., and Nagatani, R. M.: Accuracy of total ozone retrieval from NOAA SBUV/2 measurements: Impact of instrument performance, J. Geophys. Res., 99, 22975–22984, 1994.

Chandrasekar, S.: Radiation Transfer, Oxford Clarendon Press, New York, Dover, ISBN 0-486-60590-6, 1960.

DeLand, M. T., Cebula, R. P., Huang, L.-K., Taylor, S. L., Stolarski, R. S., and McPeters, R. D.: Observations of hysteresis in backscattered ultraviolet ozone data, J. Atmos. Ocean. Tech., 18, 914–924, 2001.

DeLand, M. T., Taylor, S. L., Huang, L. K., and Fisher, B. L.: Calibration of the SBUV version 8.6 ozone data product, Atmos. Meas. Tech., 5, 2951–2967, doi:10.5194/amt-5-2951-2012, 2012.

Evan, A. T., Heidinger, A. K., and Vimont, D. J.: Arguments against a physical long-term trend in global ISCCP cloud amounts, Geophys. Res. Lett., 34, L04701, doi:10.1029/2006GL028083, 2007.

Fegley, A. A. and Fowler, W. K.: Radiometric calibration of SBUV/2 instruments: retrospective Improvements, Metrologia, 28, 297–300, 1991.

Foster, M. and Heidinger, A.: PATMOS-x: results from a diurnally-corrected thirty-year satellite cloud climatology, J. Climate, 26, 414–425, doi:10.1175/JCLI-D-11-00666.1, 2013.

Frederick, J. E., Cebula, R. P., and Heath, D. F.: Instrument characterization for the detection of long-term changes in stratospheric ozone: An analysis of the SBUV/2 radiometer, J. Atmos. Ocean. Technol., 3, 472–480, 1986.

Gautam, R., Hsu, N. C., Lau, K. M., Tsay, S. C., and Kafatos, M.: Enhanced pre-monsoon warming over the Himalayan–Gangetic region from 1979 to 2007, Geophys. Res. Lett. 36, L07704, doi:10.1029/2009GL037641, 2009.

Georgiev, G. T. and Butler, A. A.: Long-term calibration monitoring of spectralon diffusers BRDF in the air-ultraviolet, Appl. Optics, 46, 7892–7899, 2007.

Gu, G. and Adler, R. F.: Interdecadal Variability/Long-Term Changes in Global Precipitation Patterns during the Past Three Decades: Global Warming and/or Pacific Decadal Variability? Clim. Dynam., 40, 3009–3022, doi:10.1007/s00382-012-1443-8, 2013.

Gurung, D. R., Kulkarni, A. V., Giriraj, A., Aung, K. S., Shrestha, B., and Srinivasan, J.: Changes in seasonal snow cover in Hindu Kush-Himalayan region, The Cryosphere Discuss., 5, 755–777, doi:10.5194/tcd-5-755-2011, 2011.

Hansen, J., Ruedy, R., Sato, M., and Lo, K.: Global surface temperature change, Rev. Geophys., 48, RG4004, doi:10.1029/2010RG000345, 2010.

Haynes, J. M., Jakob, C., Rossow, W. B., Tselioudis, G., and Brown, J.: Major characteristics of Southern Ocean cloud regimes and their effects on the energy budget, J. Climate, 24, 5061–5080, doi:10.1175/2011JCLI4052.1, 2011.

Heath, D. F., Krueger, A. J., Roeder, H. A., and Henderson, B. D.: The solar backscatter ultraviolet and total ozone mapping spectrometer (SBUV/TOMS) for Nimbus G, Opt. Eng., 14, 323–331, 1975.

Herman, J. R.: Changes in ultraviolet and visible solar irradiance 1979 to 2008, in: UV Radiation in Global Change: Measurements, Modeling and Effects on Ecosystems, edited by: Gao, W., Schmoldt, D., and Slusser, J., Springer Heidelberg Dordrecht London New York, ISBN 978-3-642-03312-4, 2009.

Herman, J. R.: Global increase in UV irradiance during the past 30 years (1979–2008) estimated from satellite data, J. Geophys. Res., 115, D04203, doi:10.1029/2009JD012219, 2010.

Herman, J. R. and Celarier, E. A.: Earth surface reflectivity climatology at 340 nm to 380 nm from TOMS data, J. Geophys. Res., 102, 28003–28011, 1997.

Herman, J. R., Larko, D., and Ziemke, J.: Changes in the Earth's global UV reflectivity from clouds and aerosols. J. Geophys. Res., 106, 5353–5368, 2001.

Herman, J. R., Labow, G., Hsu, N. C., and Larko, D.: Changes in cloud cover (1998–2006) derived from reflectivity time series using SeaWiFS, N7-TOMS, EP-TOMS, SBUV-2, and OMI Radiance Data, J. Geophys. Res., 114, D01201, doi:10.1029/2007JD009508, 2009.

Huang, L.-K., Cebula, R. P., and Hilsenrath, E.: New procedure for interpolating NIST FEL lamp irradiances, Metrologia, 35, 381–386, 1998.

Huang, L.-K., Cebula, R. P., Taylor, S. L., DeLand, M. T., McPeters, R. D., and Stolarski, R. S.: Determination of NOAA-11 SBUV/2 radiance sensitivity drift based on measurements of polar ice cap radiance, Int. J. Remote Sens., 24, 305–314, 2003.

IPCC (Intergovernmental Panel on Climate Change): Climate Change 2007: The Physical Science Basis, Cambridge University Press, Cambridge, UK, 2.9.2, 2007.

Janz, S., Hilsenrath, E., Butler, J., Heath, D. F., and Cebula, R. P.: Uncertainties in radiance calibrations of backscatter ultraviolet (BUV) instruments, Metrologia, 32, 637–641, 1995.

Jaross, G. and Warner, J.: Use of Antarctica for validating reflected solar radiation measured by satellite sensors, J. Geophys. Res., 113, D16S34, doi:10.1029/2007JD008835, 2008.

Kao, H.-Y. and Yu, J.-Y.: Contrasting Eastern-Pacific and Central-Pacific types of ENSO, J. Climate, 22, 615–632, 2009.

Kiehl, J. T. and Trenberth, K. E.: Earth's annual global mean energy budget, B. Am. Meteorol. Soc., 78, 197–208, 1997.

Kleipool, Q. L., Dobber, M. R., de Haan, J. F., and Levelt, P. F.: Earth surface reflectance climatology from 3 yr of OMI data, J. Geophys. Res., 113, D18308, doi:10.1029/2008JD010290, 2008.

Kopp, G. and Lean, J. L.: A new, lower value of total solar irradiance: evidence and climate significance, Geophys. Res. Lett., 38, L01706, doi:10.1029/2010GL045777, 2011.

Labow, G., Herman, J. R., Huang, L. K., Lloyd, S. A., DeLand, M. T., Qin, W., Mao, J., and Larko, D. E.: Diurnal variation of 340 nm Lambertian equivalent reflectivity due to clouds and aerosols over land and oceans, J. Geophys. Res., 116, D11202, doi:10.1029/2010JD014980, 10, 2011.

Norris, J. R. and Slingo, A.: Trends in observed cloudiness and Earth's radiation budget: what do we not know and what do we need to know?, in Clouds in the Perturbed Climate System, edited by: Heintzenberg, J. and Charlson, R. J., MIT Press, 17–36, 2009.

Pinker, R. T., Zhang, B., and Dutton, E. G.: Do satellites detect trends in surface solar radiation?, Science, 308, 850–854, doi:10.1126/science.1103159, 2005.

Schiffer, R. A. and Rossow, W. B.: The international satellite cloud climatology project (ISCCP): The first project of the World Climate Research programme, B. Am. Meteorol. Soc., 64, 779–784, 1983.

Schlesinger, B. M. and Cebula, R. P.: Solar variation 1979–1987 estimated from an empirical model for changes with time in the sensitivity of the Solar Backscatter Ultraviolet instrument, J. Geophys. Res., 97, 10119–10134, 1992.

Singh, A., Delcroix, T., and Cravatte, S.: Contrasting the flavors of El Niño Southern Oscillation using sea surface salinity observations, J. Geophys. Res., 116, C06016, doi:10.1029/2010JC006862, 2011.

Stevens, B. and Schwartz, S. E.: Observing and modeling Earth's energy flows, Surv. Geophys., 33, 779–816, doi:10.1007/s10712-012-9184-0, 2012.

Trenberth, K. E., Fasullo, J. T., and Kiehl, J.: Earth's global energy budget, B. Am. Meteorol. Soc., 90, 311–324, doi:10.1175/2008BAMS2634.1, 2009.

Weiss, H., Cebula, R. P., Laamann, K., and Hudson, R. D.: Evaluation of the NOAA 11 solar backscatter ultraviolet radiometer, mod 2 (SBUV/2): inflight calibration, Proc. SPIE Int. Soc. Opt. Eng., 1493, 80–90, 1991.

Wild, M., Gilgen, H., Roesch, A., Ohmura, A., Long, C. N., Dutton, E. G., Forgan, B., Kallis, A., Russak, V., and Tsvetkov, A.: From dimming to brightening: decadal changes in solar radiation at Earth's Surface, Science, 308, 847–850, doi:10.1126/science.1103215, 2005.

Wolter, K. and Timlin, M. S.: Monitoring ENSO in COADS with a seasonally adjusted principal component index, Proc. of the 17th Climate Diagnostics Workshop, Norman, OK, NOAA/NMC/CAC, NSSL, Oklahoma Clim. Survey, CIMMS and the School of Meteor., Univ. of Oklahoma, Norman, Oklahoma, USA, 52–57, 1993.

Wolter, K. and Timlin, M. S.: Measuring the strength of ENSO events – how does 1997/98 rank?, Weather, 53, 315–324, 1998.

Wylie, D., Jackson, D. L., Menzel, W. P., and Bates, J. J.: Trends in global cloud cover in two decades of HIRS observations, B. Am. Meteorol. Soc., 18, 3021–3031, 2005.